An Examination of Active Drag Reduction Methods for Ground Vehicles

Undergraduate Honors Thesis

Matthew Metka

Dr. James Gregory, Advisor

Department of Mechanical Engineering

The Ohio State University

Spring 2013

This work was supported in part by the College of Engineering and the Honda GATE Program

Abstract:

Aerodynamic drag accounts for a sizable portion of transportation energy consumption. Transportation of goods and people always involves moving objects through air, which leads to a force opposing motion. This force can account for more than 60% of power consumed by a ground vehicle, such as a car or truck, at highway speeds. There is a wide range of drag coefficient seen on ground vehicles with a strong correlation to vehicle shape. The shape of the vehicle is often determined by functional necessity, which places a limit on vehicle aerodynamic improvements. It is desirable to increase the aerodynamic performance of a vehicle with little penalty in functionality, which leads to the investigation of active flow control methods. Active flow control methods can involve a type of air jet at critical locations on the vehicle shell and require little to no shape modification. The focus of this experimental study is drag reduction on an Ahmed body vehicle analogue using a variety of configurations involving fluidic oscillators to promote attachment and reduce wake size. A fluidic oscillator is a simple device that converts a steady pressure input into a spatially oscillating jet. This type of actuator may be more efficient at influencing the surrounding flow than a steady jet. The model is tested in the OSU subsonic wind tunnel. Changes in drag are measured using a load cell mounted within the vehicle model. Different flow visualization methods are used to characterize the flow structure changes behind the model. A 7% drag decrease is realized with the 25^{o} spanwise oscillator array configuration, attributed to the reduction of the closed recirculation bubble size. Testing shows that attachment is promoted on high angle configurations with a Coanda surface and steady blowing however this leads to a drag increase, possibly due to the formation of longitudinal vortices. This indicates that future methods must include vortex control in conjunction with separation control to achieve a net base pressure increase on the high angle slant configurations.

Acknowledgments:

I would like to thank Professor Gregory for his time and efforts in support of this project. This has been a highlight of my undergraduate education and I greatly appreciate the opportunity to work on this. I would like to thank Mehmet Tomac, whose assistance and contributions were essential for the extent of this project. Thanks to Samik Bahattacharya for his assistance in setting up PIV, which adds another dimension to the analysis. Thanks to Stewart Benton for helping with the hotwire measurements. I also thank the numerous other students, staff, and faculty that have provided assistance along the way. I want to thank the College of Engineering and the Honda GATE program for their financial contributions. Finally, I want to thank my parents who afford me the opportunity to attend college.

Table of Contents:

Figures:

Tables:

Background:

Aerodynamic drag is the aerodynamic force that opposes motion and accounts for a large fraction of transportation energy consumption across all sectors. For the ground vehicle sector, this is particularly important due to the large number of vehicles being driven globally. At highway speeds, more than 60% of the useful energy input into the vehicle is dissipated to overcome drag.[1] The drag force of the vehicle can be reduced by altering the shape of the vehicle. In many cases the need for a particular form, due to aesthetics or for a specific functionality such as cargo capacity or visibility, overrules the desire to minimize drag. This design hierarchy makes active flow control methods appealing to the automotive engineer. An active flow control method uses an energy source to alter the flow around a vehicle. Active methods may potentially be implemented with little to no perceptible change in shape, which is one reason why this method is attractive. It is required that the energy input to the actuator be low enough such that a true gain in efficiency can be claimed. This project examines several actuator configurations using fluidic oscillators on a vehicle model to attempt large-scale changes in the flow and ultimately reduce drag.

Drag is the result of interaction between the vehicle shell and the surrounding air molecules caused by relative motion between the air and vehicle which results in a net force opposing motion. From the ground reference frame it is clear that air molecules are accelerated from rest in the direction of vehicle motion due to viscous and pressure interactions. This requires additional energy to be provided by the engine. It is interesting to note that on the highway more than half of the useful energy output of the engine is used to accelerate and heat the surrounding air molecules.[1] The remaining energy consumption is due to rolling resistance, drive train inefficiencies, and onboard systems such as air conditioning.

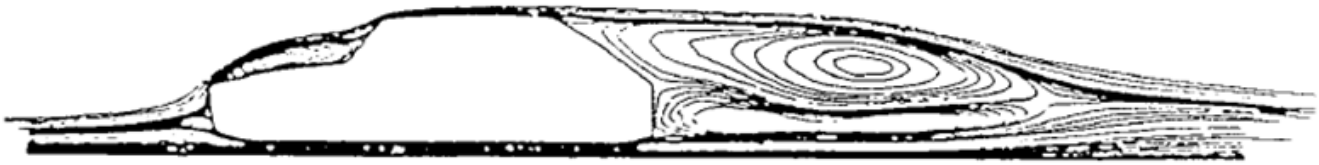

Figure 1: Example ground vehicle wake, which contributes to the majority of drag force.[14]

The two sources of drag are skin friction, which is the result of viscous interaction on the vehicle skin, and pressure drag, which is due to the net pressure difference between the front and rear of the vehicle. The dominant component of drag on road vehicles, as with most bluff bodies, is pressure drag, which is estimated to account for more than 90% of the total drag.[5] The primary source of pressure drag is the unsteady separated wake at the rear of the car, shown in Figure 1, which leads to net lower pressure on the back of the car than on the front.

The drag force depends on the airspeed squared, so with all else being equal the drag will increase by a factor of four when the speed is doubled. Drag also depends on the frontal area, air density, and most importantly for this study, the drag coefficient. The drag coefficient is a measure of the aerodynamic efficiency of a shape. The drag coefficient is defined in Eq. 1, where F_D is the drag force, V_∞ is the airspeed, ρ is the air density, and A is the frontal area. It is generally found by experimentally measuring the drag force.

$$C_D \equiv \frac{F_D}{\frac{1}{2}\rho V_\infty^2 A} \qquad (1)$$

A drag coefficient sampling of common vehicles along with the estimated drag force at highway speed (65mph) is given in Table 1.

Table 1: Drag coefficient of several production vehicles[11]

Vehicle	C_D	Frontal Area (ft^2)	Estimated Drag Force at 65 mph (lbs)
2004 Prius	0.26	24.00	67
2001 Civic	0.36	20.39	79
2005 Ford Escape	0.40	29.00	125
2003 Hummer H2	0.57	46.49	286

It is clear that there is a wide range in aerodynamic efficiency between vehicles. Much work has been done in recent years to reduce the drag coefficient for production road vehicles due to increasing awareness of the environmental, financial, and geopolitical implications associated with transportation fuel use. Several methods for improving the efficiency include optimizing details such as mirrors and corner radii, tapering the rear of the vehicle to reduce that area on which separated flow acts, and other shape modifications that eliminate local areas of separation. Also, decreasing the ground clearance will generally decrease wake size and lead to lower drag.[4]

In most production vehicles the component of the drag coefficient from the front of the vehicle is generally much less than the total drag coefficient.[1] Although there is a stagnation region on the front of the vehicle, there are also low pressure areas on rounded corner radii and other regions that result in the average pressure on the front of the vehicle being very close to ambient atmospheric pressure, so most of the research is focused on the unsteady wake at the rear.

There are different active and passive flow control devices and methods that operate with the goal of reducing drag by delaying separation, altering the vortex structure, and increasing the pressure acting on the rear of the vehicle. These may be added to an existing vehicle or

incorporated into vehicle design to reduce drag further than conventional methods allow. A passive device is defined to be one whose mechanism depends solely on the free stream kinetic energy to alter the flow. An example of a passive device is a small fin structure placed upstream of the point of separation, used to generate vortices that increase the energy of the boundary layer. An active device is defined to be one that uses an external energy source to alter the flow. An example of an active device would be an array air jets powered by an onboard pump. The goal of flow control actuators is to enact large scale changes in a flow field with minimal energy input.[6] Active and passive methods may individually consume energy, however the net effect of the device is to reduce the total energy consumed by the vehicle.

The goal of this research is to begin to assess the efficacy of fluidic oscillators for drag reduction on the Ahmed body vehicle model, Figure 3. The study examines various configurations that use fluidic oscillator at the rear of the Ahmed model to reduce drag by controlling the unsteady wake. A fluidic oscillator is an interesting device that contains no moving parts, Figure 2, and converts a steady flow input into a sweeping and oscillating jet due to an unsteady internal mixing process. The frequency of the oscillation can range between several hundred and tens of thousands of hertz depending on geometry and flow rate. The benefit of this device is that a larger region of flow can potentially be influenced for a given energy input compared to other actuation methods. The big picture goal of this study is to contribute towards understanding and development of active flow control for ground vehicles and eventually lead to the implementation of such techniques on production vehicles.

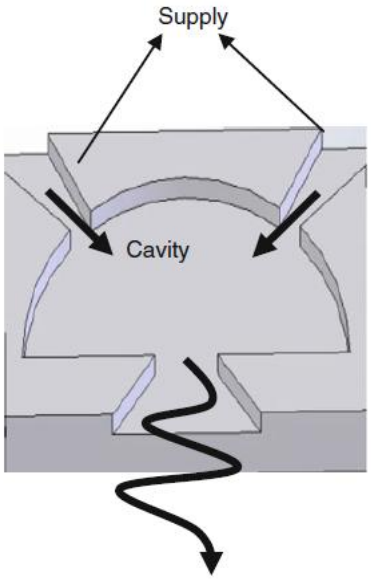

Figure 2: Fluidic oscillator cavity.[15]

Figure 3: Ahmed Model in the wind tunnel.

Experimental Approach:

Ground vehicle aerodynamic research is often done on a simplified vehicle model called the Ahmed body, originally proposed by S. Ahmed. The current use of this model allows results to be compared with other studies. The Ahmed model, depicted in Figure 4a, has the potential to generate a complex wake that resembles that from an actual road vehicle. The specific flow structures in the wake depend on the rear slant angle, indicated by θ. The goal of this shape is to keep the flow attached on the front of the model while allowing a complex wake to form at the rear.

The drag coefficient of the Ahmed model is strongly dependent on slant angle, as seen in Figure 4b. At slant angles less than 30 degrees the flow remains partially attached to the slant face and longitudinal vortices form on each edge. These vortices have the effect of creating a local region of low pressure, which is detrimental, while also providing the benefit of downwash that helps keep flow attached to the slant.

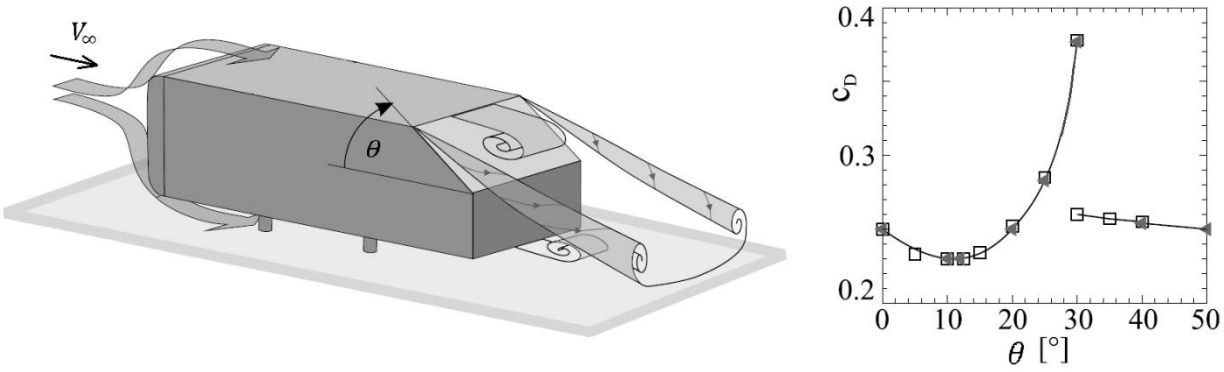

Figure 4: a.) Ahmed model and b.) Drag coefficient as a function of slant angle (Adapted from Brunn et al.)[9]

A minimum drag is reached at 15 degrees, where an optimum balance is found between vortex strength and the area on which separated flow acts.[2] As the angle is increased beyond 15^o, the increasing strength of the longitudinal vortices and size of the closed separation bubble on the slant leads to a higher drag. At 30^o the flow randomly oscillates, with mean period on the order of 30 seconds, between a high drag state characterized by a closed recirculation bubble on the slant and longitudinal vortices and a fully separated low drag state with no vortices.[2] At angles greater than 30^o the flow remains fully separated, with relatively low drag.

This study examines drag reduction methods for the 25^o, 45^o, and 90^o slant angle configurations. The 25^o configuration is intended to represent the flow on a typical sedan class vehicle. The baseline wake of this configuration naturally contains a closed separation bubble, which reattaches at the bottom third of the slant, and longitudinal vortices that form on the sides edges. This configuration has a relatively high drag of 0.29, as seen in Figure 4b.

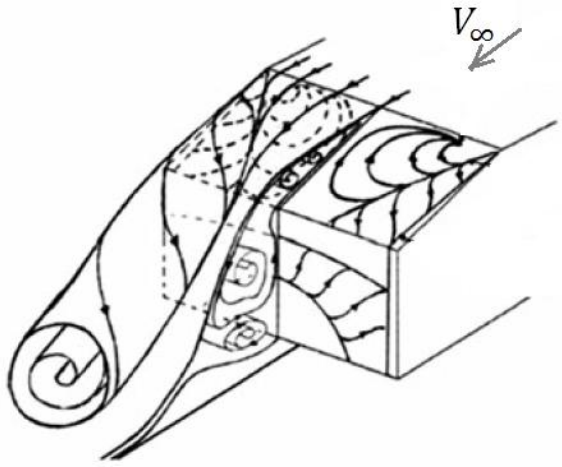

Figure 5: Baseline Flow on the 25 degree Ahmed Model (Adapted from Joseph et al.)

The 45^o angle is selected to represent flow on a typical hatchback or crossover SUV configuration. This base flow is described as fully detached with two span wise recirculation regions forming on in the wake. Figure 6 shows that baseline flow behind a 35^o Ahmed model which is qualitatively similar to the 45^o. The upper vortex is due to flow from the top of the model and the lower is driven by flow from beneath the model. When viewed from behind, the recirculation structure resembles a torus due to flow from the sides resulting in similar recirculation. The drag coefficient of 0.26 for this case is actually lower than the 25^o due to the elimination of the highly dissipative closed recirculation bubble and longitudinal vortices.

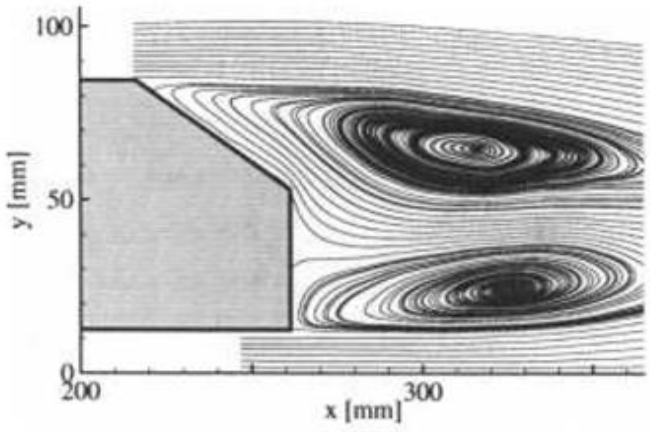

Figure 6: Baseline flow on the 35^o Ahmed model (Adapted from Brunn et al.)[9]

The 90^o angle represents flow that may be seen on a semi truck. This flow is fully detached with a large wake length. The baseline drag of this setup is 0.25, which is lower than both the 25^o and 45^o configurations. Each of these setups are expected to behave differently when active methods are applied.

The goal of actuation is to increase the average base pressure on the model. The pressure at a particular location is generally expressed in terms of the pressure coefficient C_p, defined in Eq. 2, where p is the pressure, p_∞ is the ambient pressure, V_∞ is the airspeed, ρ is the air density.

$$C_P \equiv \frac{p - p_\infty}{\frac{1}{2}\rho V_\infty^2} \qquad (2)$$

Due to the weak contribution of skin friction on the Ahmed model, the drag coefficient can be approximated by Eq. 3, where A is the projected area perpendicular to the direction of motion. The pressure coefficient integrated on the projected frontal and rear areas to give a drag coefficient that neglects viscous effects.

$$C_D \approx \frac{\iint_{Front} C_p \, dA - \iint_{Rear} C_p \, dA}{A} \qquad (3)$$

It was shown by Lajos that the C_D contribution from the front of a shape such as this can be less than 0.01.[8] This is partially due to the suction peaks at the front corner radii, Figure 7, where $C_p$is shown to reach a minimum of -1.5. This results in the average pressure coefficient on the front being close to zero.

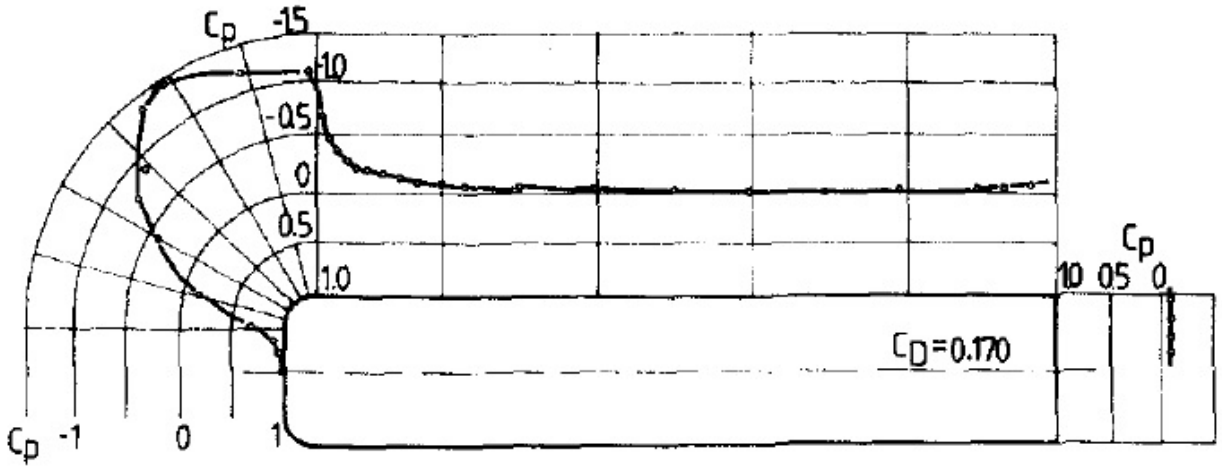

Figure 7: Pressure distribution on a rectangular bluff body.[8]

With this taken into consideration the drag coefficient of the Ahmed model is estimated as the average pressure coefficient, $\overline{C_p}$, on the rear slant, Eq. 4

$$C_D \approx -\frac{\int_{Rear} C_p \, dA}{A} = -\overline{C_p} \qquad (4)$$

The pressure on the slant is not directly measured in this study. This discussion simply illustrates the primary source of drag on the Ahmed model. On a real vehicle, there will be contribution of drag from sources such as mirrors, underbody protrusions, and other complexities that are not accounted for in the Ahmed model. Although it still represents the primary source of drag, the unsteady wake, with fidelity.

An example of how flow control can affect the pressure distribution on a 25^o slant angle is shown in Figure 8a. An impressive reduction of 17% has been achieved by Ruomeas et al. in a CFD study by eliminating the closed separation region with a suction slot at the top of the slant.[3]

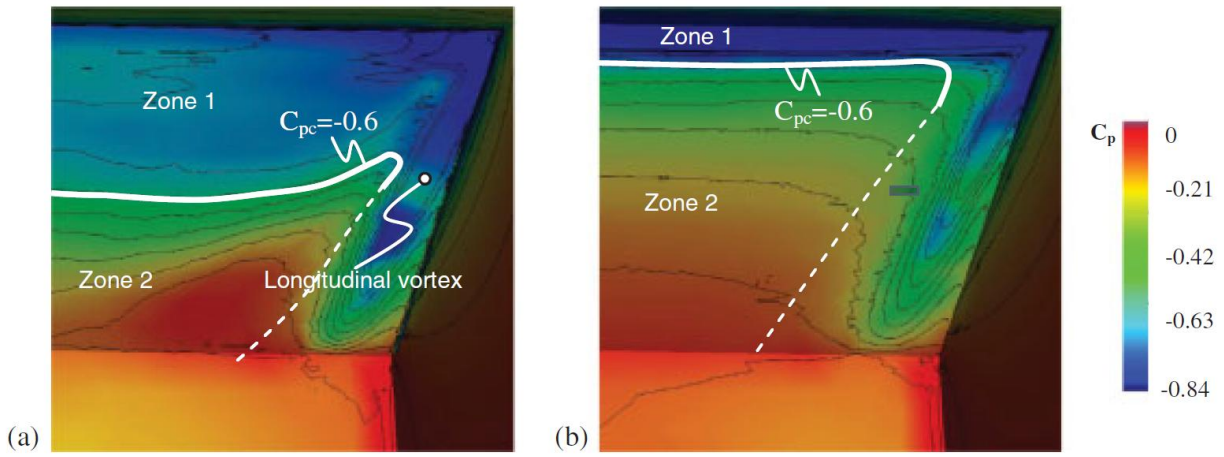

Figure 8: Pressure distribution on the back of the model (25° slant), **a** is baseline, **b** is with control [3]

Figure 8b shows that the suction locally decreases the base pressure at the top edge of the slant, however the elimination of separation results in a higher pressure on the rest of the slant, which results in a drag decrease of 17%.[3] This also has the effect of reducing the strength of the longitudinal vortices that depend on the relatively low pressure of the slant to form.[3] This illustrates the effect flow control can have on drag.

Coanda Surface

Flow detachment, which is generally unfavorable, is attributed to insufficient flow energy to overcome the adverse pressure gradient experienced at the rear of the model. A setup based on the Coanda effect is used to prevent separation at the roof end. The Coanda effect can describe the attachment of flow to a curved surface when there is a locally higher velocity than the surroundings. This is the result of a balance between the low pressure created by the centripetal acceleration of fluid particles and the surrounding higher pressure ambient air. The current use of the Coanda surface is to create local region of low pressure, which helps the flow attach to the slant. The jet energy also provides the additional flow energy, which was lost due to skin friction, needed to overcome the adverse pressure gradient on the slant. The intention is

that a net base pressure increase will be experienced due to pressure recovery further down the slant, despite the local suction on the Coanda surface. This method has proven successful in 2-D studies using Coanda surfaces and air jets to promote attachment to the rear surface, which ultimately led to a 10% drag reduction.[5]

A Coanda surface is created at the interface of the roof and rear slant, where the flow typically detaches. An array of 9 fluidic oscillators, spaced at 34 mm from center to center, blow tangentially onto the Coanda surface. The resulting jet outflow attaches to surface and entrain the surrounding fluid onto the slant. The selected Coanda radius and jet spacing are selected as a first pass partially based on geometrical constraints. These parameters can be optimized in subsequent studies. The setup on the 45^{o} case is shown in Figure 9b. The configurations are similar on the 90^{o} and 25^{o} slants.

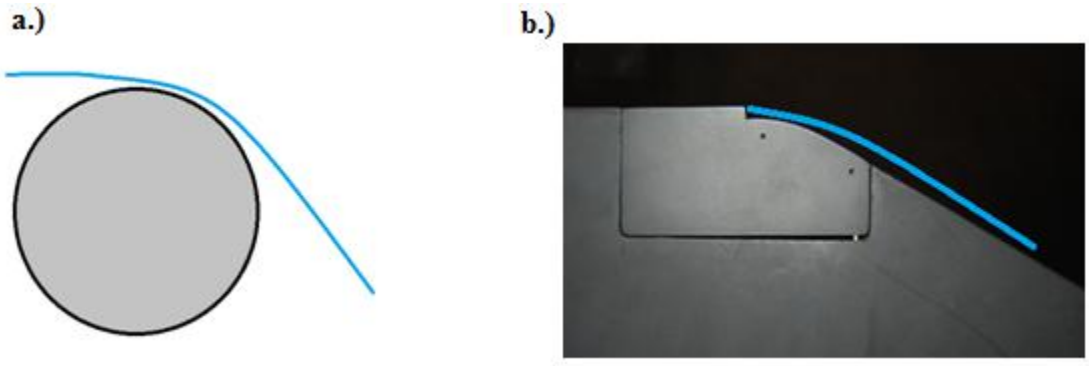

Figure 9: a.) Coanda effect on a cylinder, **b.)** Coanda surface on the Ahmed slant.

Periodic Excitation

Another method for reducing drag involves exciting the shear layer to amplify vortices that are naturally shed from the model. It is intended that larger vortices will increase mixing between the boundary layer and the surrounding high velocity flow, which decreases the

boundary layer energy deficit and allows attachment. The method works by enhancing natural instabilities in the boundary layer that result from velocity gradient between the surface of the model and the fast moving air above. The instabilities can be amplified to form a vortex by introducing a pulse of air where the shear layer detaches. The instabilities naturally form vortices at the separation line with a wavelength similar to the height of the model.[9] Periodic forcing can cause the phase of shedding to match the pulse phase when close to this natural frequency, which allows the jet outlet to amplify vortices. An explanation of the feedback mechanism between shear layer instabilities and vortices is shown in Figure 10.

A notable 27% drag reduction is witnessed using synthetic jets at the line of separation on a 35^{o} Ahmed model in a study by Brunn. et al.[9] In this 2-D water channel study, excitation near the natural shedding frequency at $St = 0.2$ results in amplification of the vortices and greater turbulence as seen in Figure 12. This leads to delayed separation and significantly decreased wake length, Figure 11. This study illustrates the potential of periodic excitation for reducing dra. A much lower energy input is expected for these types of methods than steady methods such as the Coanda surface.

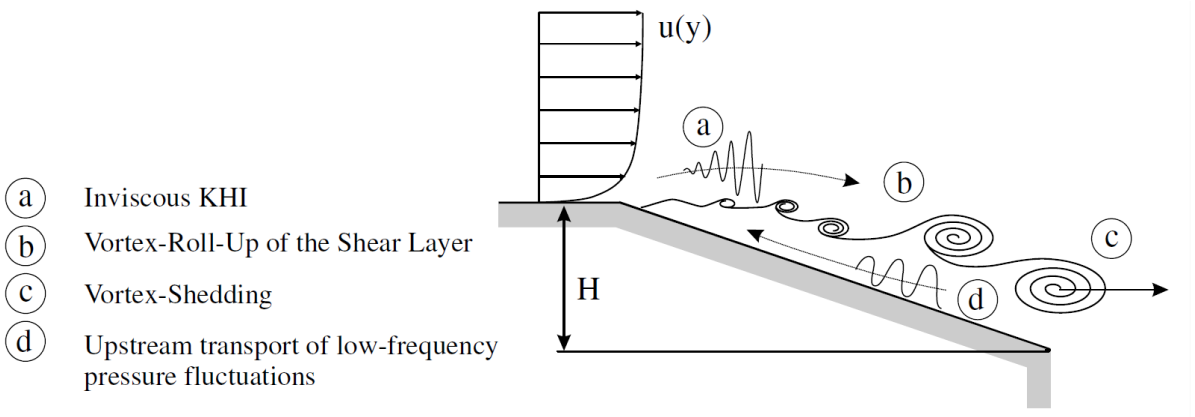

Figure 10: Kelvin Helmholtz instability and vortex shedding from the rear slant**.**

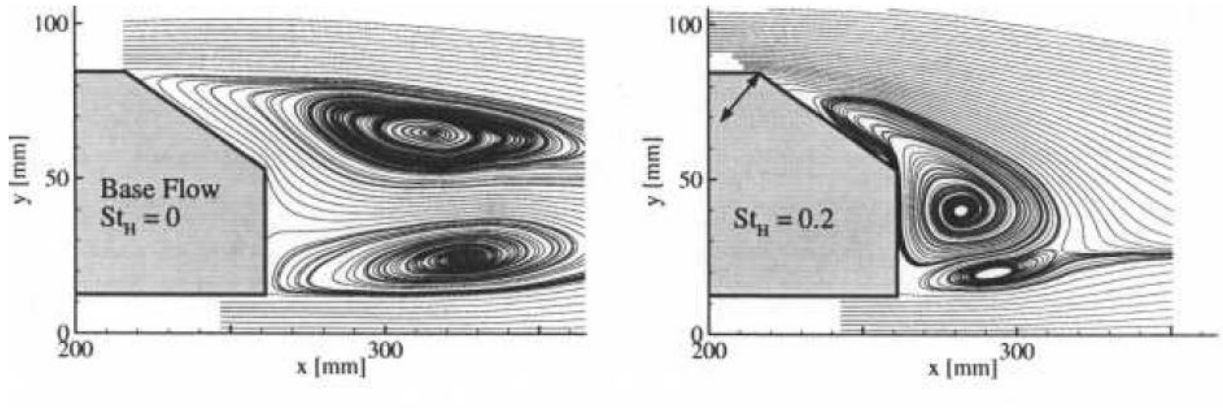

Figure 11: Baseline flow **a,** and forced flow **b** behind a 35° Ahmed model.

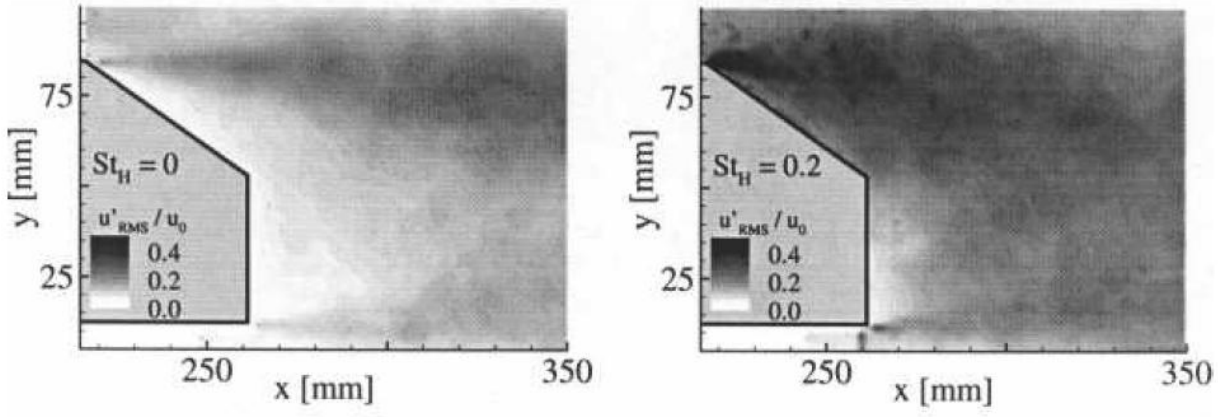

Figure 12: Turbulence level with forced and unforced flow on a 35° Ahmed model.

Successful attempts have been made at periodic excitation on the 25° Ahmed model, which does not contain fully separated flow.[10] The mechanism behind drag reduction on this slant is generally more complicated than on the fully separated cases. Joseph et al. placed a line of pulsed air jets normal to the surface on a 25° Ahmed model and showed that the response depends on the drag reduction mechanism that the actuator excites. Figure 13a shows the result when the acutator is placed slightly ahead of the rear slant on the roof. Acutation from this location results in a size reduction of the closed recirculation bubble.[10] This type of acutation strategy is strongly dependent on acuation frequency. When actuation is placed at the top of the

slant, the resulting modification of the wake leads to an increase in base pressure on the back vertical surface, indicating a change in the torus structure.[10] This strategy shows a little frequency dependence, Figure 13b. Drag decreases of 8% have been achieved with both actuation locations, but the second method is more efficient, indicated by lower C_μ in Figure 13b.[10]

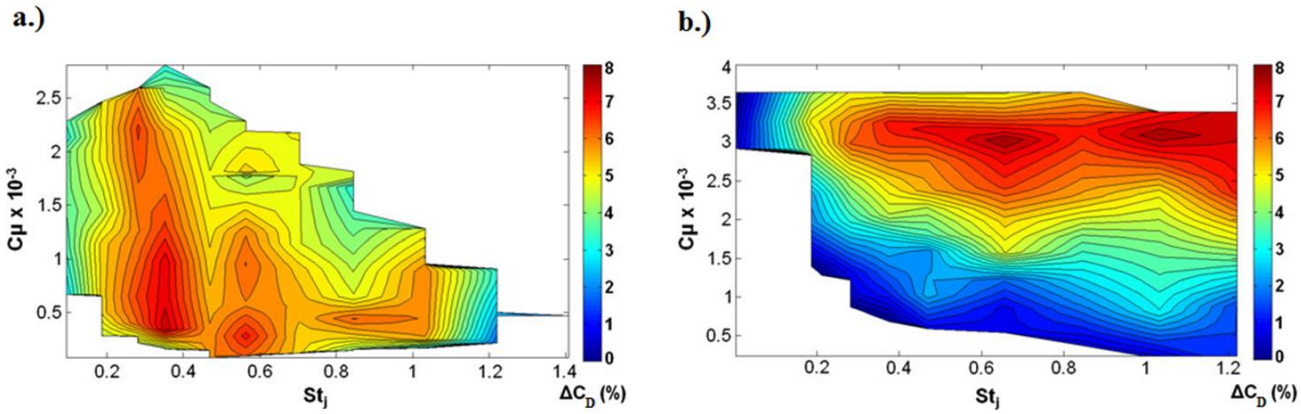

Figure 13: Drag reduction as a function of flowrate and frequency on the 25° slant with periodic forcing. **a** is the result using a discontinuos slot at the roof end. **b** is with a continuous slot at the slant top edge.[10]

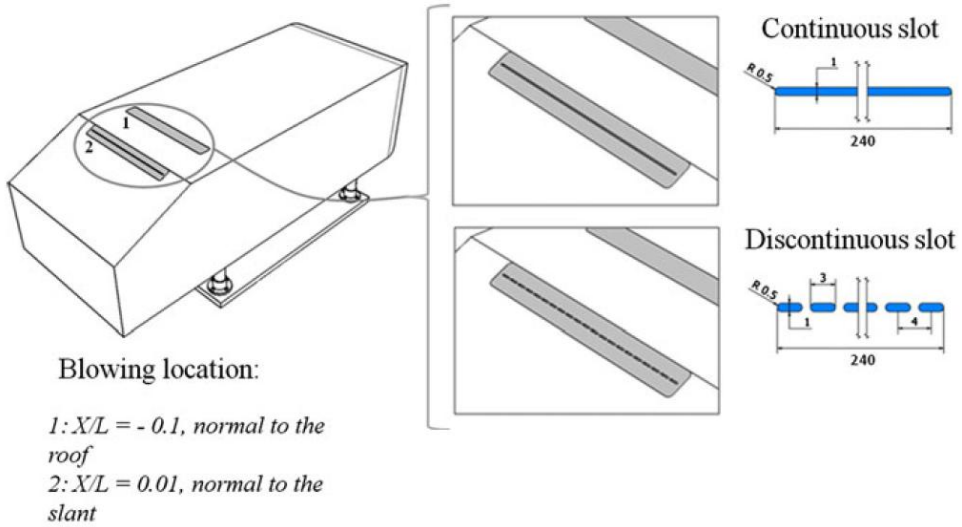

Figure 14: Actuator configurations used by Joseph et al. The configurations are used separately.[1]

Spanwise Oscillator Array- SOA

Periodic excitation is attempted with a spanwise array of fluidic oscillators, referred to as SOA, along the slant edge. Figure 15a shows the array mounted on the 25^{o} configurations. Located immediately at the slant edge boundary, the array is expected to influence both the torus structure and the closed separation bubble. The gap between the array and the surrounding surfaces is filled with plumbers putty and trimmed to reduce potential separation inducing discontinuities, Figure 15b. The array, containing 8 fluidic oscillators, can be mounted at various angles relative to the free stream slant surface and glued into place.

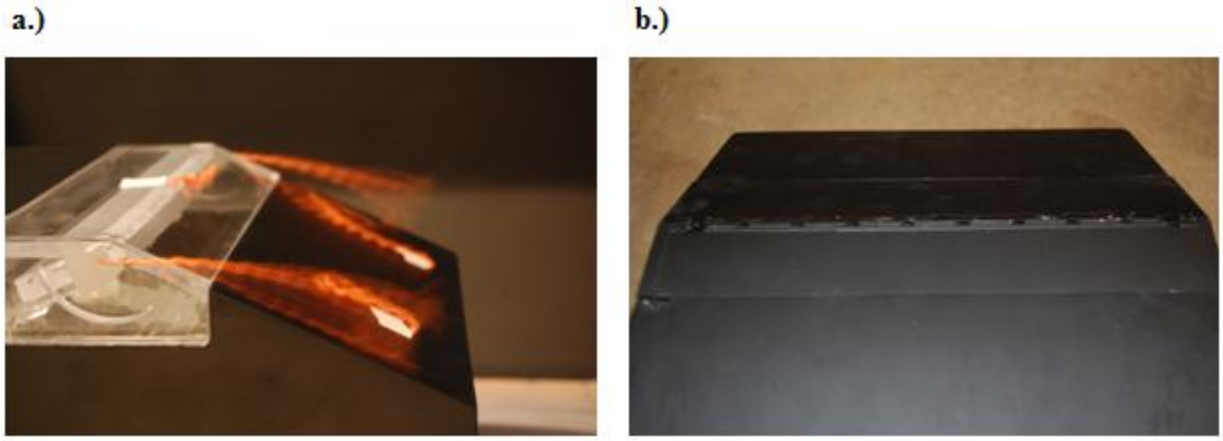

Figure 15: SOA configuration on the 25^{o} Ahmed slant. **a** shows how the actuator is mounted in the model. **b** shows the configuration during testing, which includes clay putty to reduce discontinuities.

This array is examined under steady and pulsed conditions. The pulsed condition is accomplished with a binary solenoid valve to gate the pressure supply to the array. One goal of the valve is to excite periodic flow phenomena in a coherent manner, compared to the incoherent signal due to random phase between individual oscillators. The other goal of the solenoid is to decouple actuation frequency from flow rate. The frequency of the oscillators can be increased

with flow rate, but this limits the operating range to a line on the flow rate-frequency plane if one oscillator scale is used. Drag reduction was previously shown to be a function of both flow rate and frequency.[10] Decoupling the two is important for determining the change in drag as a function of forcing frequency.

The drag response between forcing frequency 5 Hz and 150 Hz is examined in 5 Hz increments. This is in the Strouhal range that the previously mentioned studies have seen the greatest effect at the testing airspeed of 24 m/s. Several flow rates will be used at each frequency, as drag reduction has been shown to be a function of both. The performance under steady non-gated conditions will also be measured. Drag is directly measured with a load cell built into the model.

Flow Control Actuators

A relatively new type of flow control actuator called a feedback free fluidic oscillator is used exclusively in this study. A fluidic oscillator is a simply device that generates a periodic sweeping jet at the outlet, Figure 16. The oscillation is due to an unsteady internal mixing process between the two jet inlets within a chamber, Figure 17. An oscillation will develop with little dependence on the exact mixing chamber geometry. The resulting outlet jet oscillates with a frequency ranging from several hundred to several thousand hertz.[6] The frequency of oscillation depends on

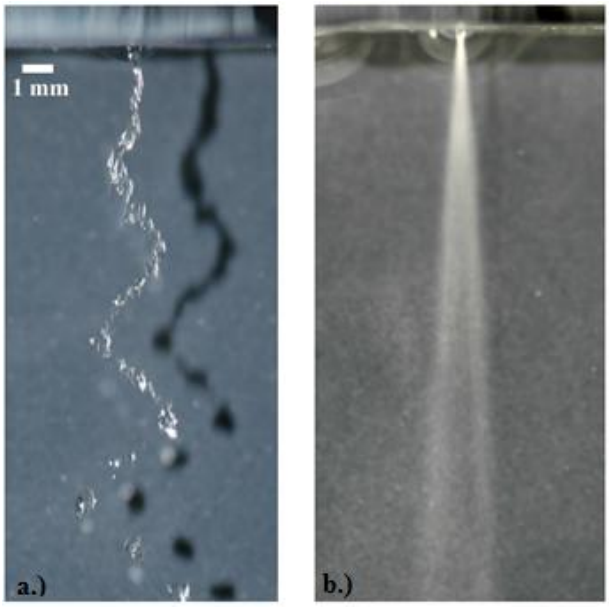

Figure 16: Instantaneous **a** and time averaged output **b** from a fluidic oscillator using water as the working fluid.[6]

geometry and flow rate. Gregory et al. showed that the frequency increases linearly with flow rate over most operating conditions.[6] The frequency also increases as the geometry is scaled down.

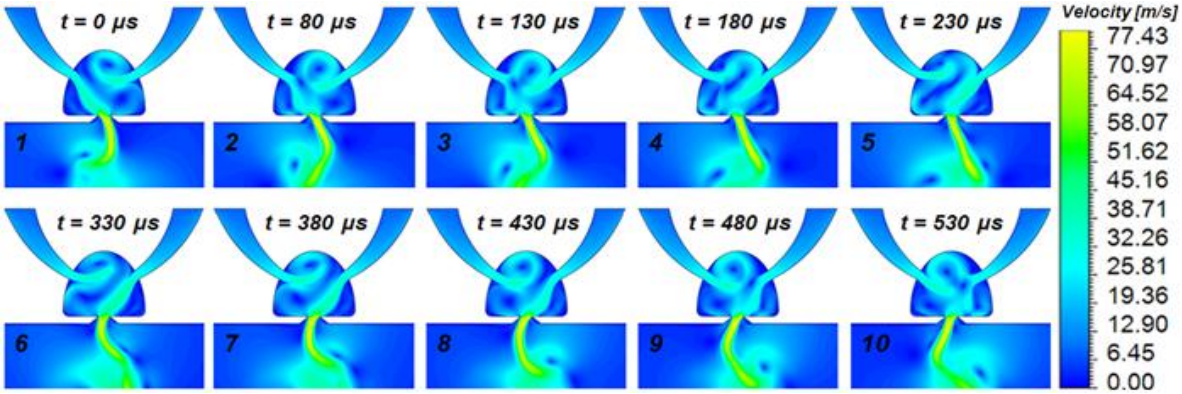

Figure 17: Internal jet interaction, (Tomac and Gregory 2012)

One benefit of this type of actuator is that due to the sweeping motion of the oscillator jet a larger region can be influenced for a given flow rate, compared to traditional slot blowing. This is desirable because the net energy savings from drag reduction depends on the actuator energy consumption, which is proportional to flow rate and supply pressure. This is the first study in which a feedback free fluidic oscillator is used on the Ahmed body model as far as the author is aware.

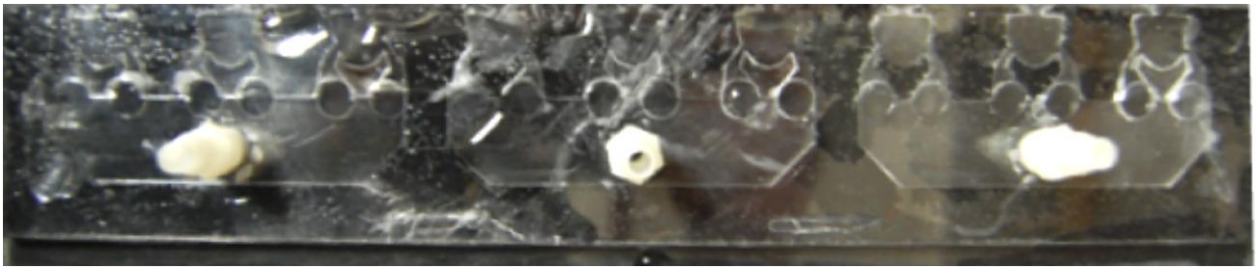

Figure 18: Oscillator array used for the Coanda configurations.

Experimental Setup:

Ahmed Model (Test Article)

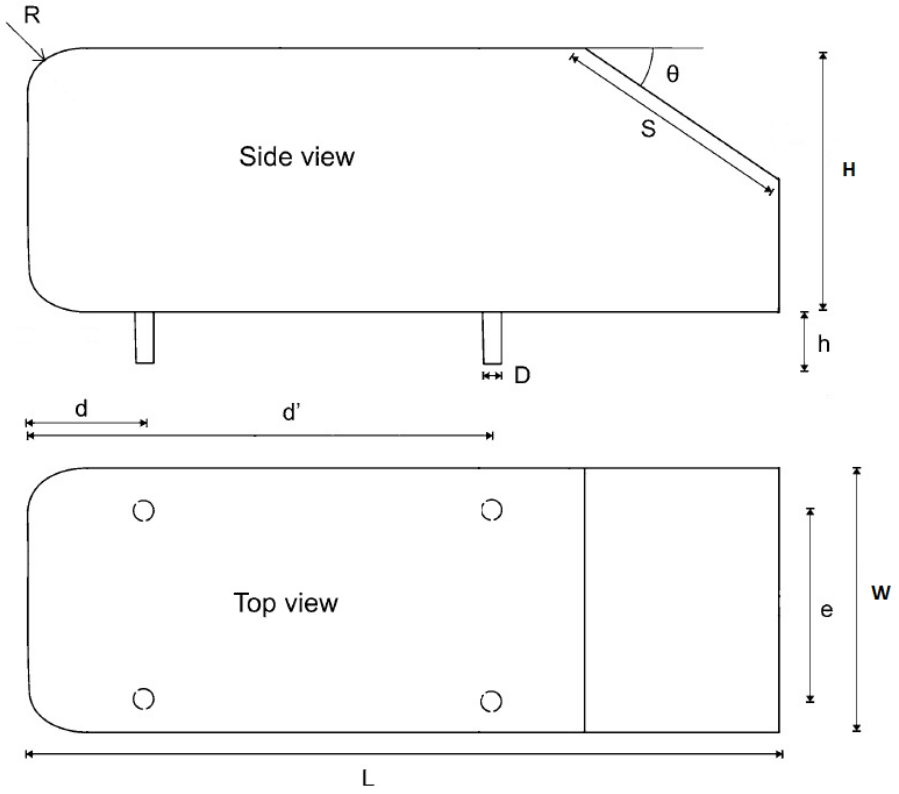

Figure 19: Ahmed model section view, (adapted from Conan et al.)[12]

Table 2: Ahmed Model Dimensions

Symbol	Description	Measured Dimension	% Deviation from Ahmed
L	Total Length	$869 \pm 2\ mm$	0.3
W	Total Width	$320 \pm 2\ mm$	-1.1
H	Height	$239 \pm 2\ mm$	-0.4
h'	Support Height	$45 \pm 2\ mm$	8.4
S	Slant Length	$184 \pm 2\ mm$	-0.1
R	Front Radius	$83 \pm .5\ mm$	0.0
d	Support Distance 1	$181 \pm 2\ mm$	8.0
d'	Support Distance 2	$531 \pm 2\ mm$	-4.8
D	Support Diameter	$25 \pm .5\ mm$	0.4
e	Support Spacing	$246 \pm 2\ mm$	-0.2
θ	Slant Angle	$25\ ,45, 90 \pm .5\ degrees$	-

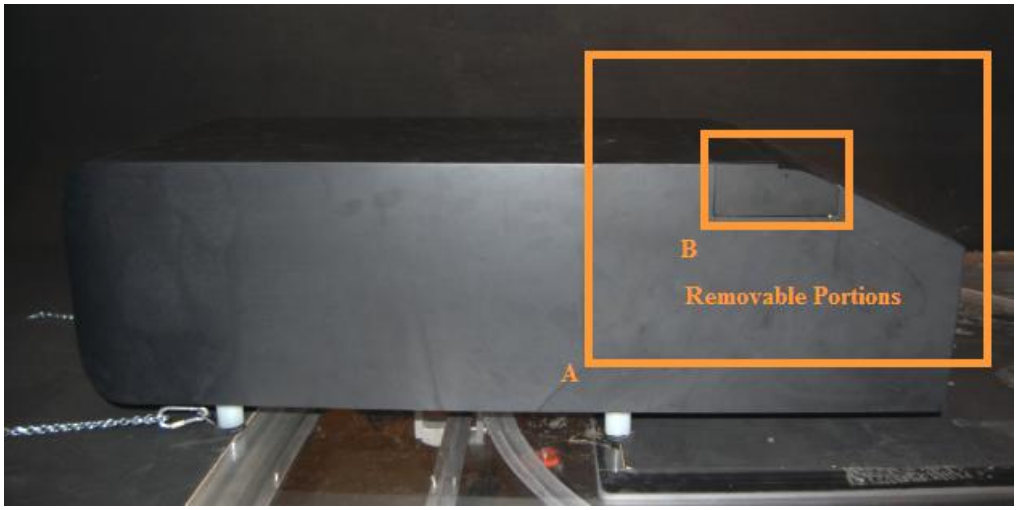

Figure 20: Ahmed model with removable sections.

This research is done on an traditional Ahmed model scaled by 0.83 for a lower test section blockage. The frontal area of the model is 0.079 m^2, leading to a blockage of 5.7%. This is higher than other studies, typically less the 3%, however making the model smaller would require higher tunnel speeds for the desired Reynolds number and make construction of the model more difficult as the required tolerances would decrease. The dimensions of the model are given in Table 2. The model and associated components were designed and built specifically for this project. The rear part of the model is removable to allow different slant angle pieces to be interchanged, Figure 20 cutout A. The interface between the model base and the rear has a step height less than 1 mm between the two and gap less than 3 mm wide. The interface must be even to minimize the risk of introducing boundary layer disturbances. The rear slant pieces slide into the model base and are secured with two screws on the back of the model. The 25^o,45^o, and 90^o slant configurations are built to represent the flow types mentioned earlier. The actuator assemblies may be removed from these slant pieces, Figure 20 cutout B, to allow the different actuation methods to be tested on the same slant piece. This reduces the number of parts that

must be constructed. Further details on the Ahmed body setup and pictures of the different actuator configurations can be found in the Appendix.

Flow Control Actuators

The actuators used in this study are arrays of feedback free fluidic oscillators, custom designed for this application. The oscillator geometry is based on previous research done by Gregory and Tomac, of the OSU Mechanical and Aerospace Engineering department. An example array is shown in Figure 18, notice that there are three sectors on the array to allow forcing to be different on the edges than in the middle of the slant. In the current study, the flow rate to each oscillator in the array is the same. Flow rate to the array is measured on a time-averaged basis for steady and unsteady actuation using an Omega air flow meter capable of rates up to 100 L/m. The uncertainty of flow measurements is around 3 L/m, based on the 3% FSO rating. Flow rate on the pulsed cases is not constant but the reading is assumed to give an average flow rate. The flow meter is placed before the solenoid, and is used to control flow rate also with the built in valve. The actuation system is powered by 90 psi shop air. The pressure drop at the array is generally much lower, however there is significant pressure loss before the array. Losses due to piping, solenoid, and valves can be reduced considerably with optimization of these components, actuator energy consumption in this case will be based from the jet exit velocity and represented with a dimensionless parameter, C_μ, which is defined later.

The actuator pieces are laser cut from acrylic, using CAD designs, and the arrays formed by gluing together several 2D cutouts. The oscillator chambers are made from 2.5 mm thick acrylic. The selection of chamber thickness controls the frequency and velocity characteristics of a jet as a function of flow rate. A lower thickness will generally result in higher frequency and

higher velocity sweeping jets at a given flow rate, while a greater thickness has the opposite effect. This thickness is selected as a first pass. It may be beneficial to select a lower thickness in future experiments to achieve higher exit velocities.

The maximum jet exit velocity as a function of flowrate to the SOA array, which contains 8 actuators, is shown in Figure 22. This is based on a steady un-gated air supply to the array. The jet velocity is measured with a constant temperature hotwire anemometer 4 mm from the outlet in the orientation shown in Figure 21.

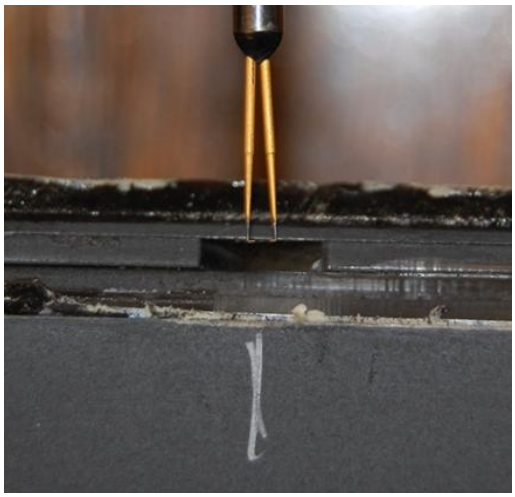

Figure 21: Hotwire measurement location.

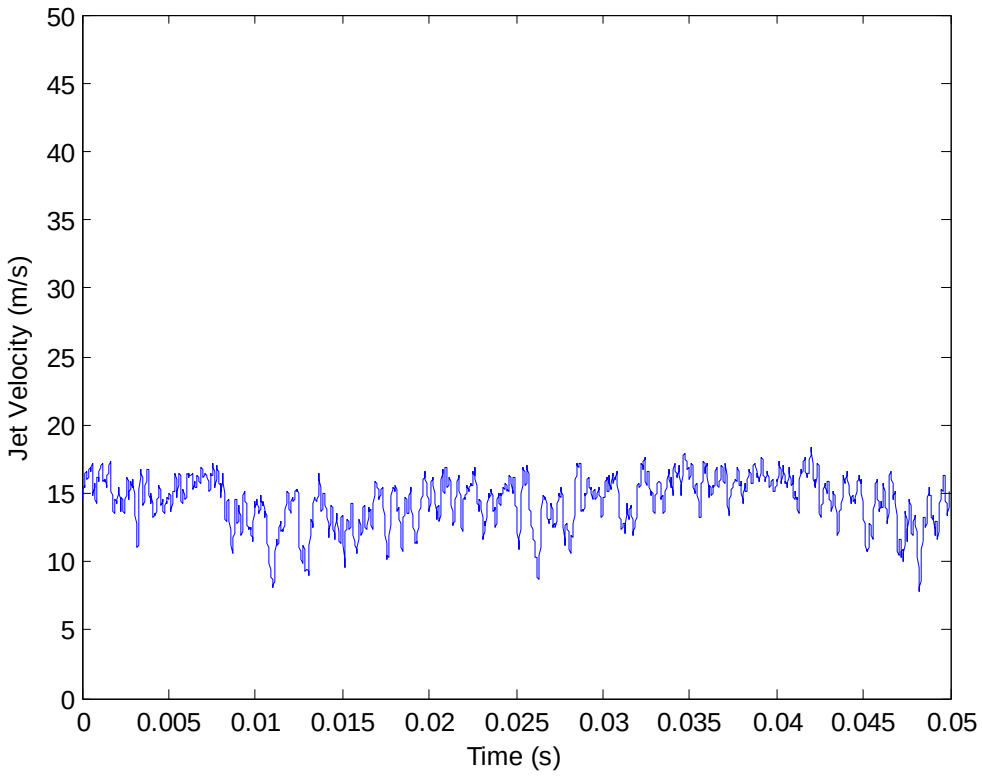

Figure 22: Velocity measured at 2mm above the center of an oscillator in the array of eight oscillators. The unsteadiness is due to the sweeping motion of the oscillator, 35 L/min.

Periodic excitation is achieved by gating the air pressure supply to the array. A Parker Hannifin #009-0089-900 normally closed solenoid valve with a 0.116" orifice, is placed inside the model and connected to the array with roughly 16" of 3/8" vinyl tubing. Placing the solenoid inside the model is done to minimize the amount of fluid capacitance beyond the valve, which would attenuate the signal being sent to the shear layer. The valve is rated at a response time of less than 5 ms, which should allow for gating up to ~150 Hz. The valve is driven with an Iota One pulse generator that is controlled with an Agilent signal generator. The signal generator creates a 5V square wave, which activates the Iota One, and allows frequency and duty cycle to be easily controlled. An example signal from the gated array is shown in Figure 23. This velocity contains the high frequency fluidic oscillator signal superimposed on the 40 Hz square wave gating signal, also indicated in the figure.

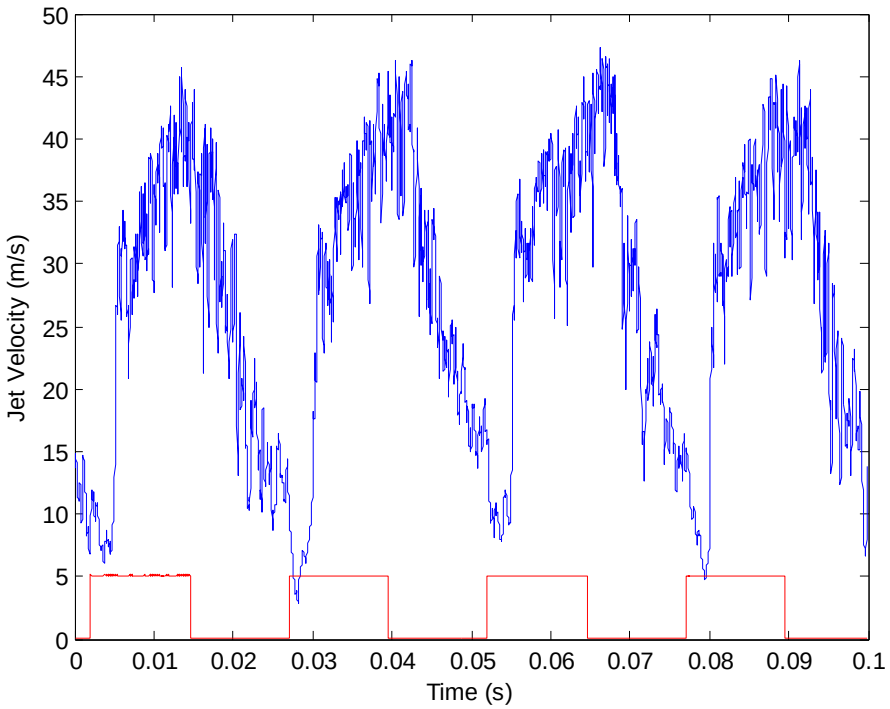

Figure 23: Gated array jet velocity, 40 Hz, 50% Duty Cycle, ~35 L/min average flow rate.

Notice that the jet velocity does not reach zero at 40 Hz , despite a closed solenoid 50% of the time. This is due to the fluid resistance and capacitance within the array and supply lines. As frequency increases the effect of RC becomes more apparent. Figure 24 shows the velocity with a 100 Hz gating frequency, at the same mean flow rate as in Figure 23. The amplitude of the gated oscillation is lower at 100 Hz. The maximum velocity decreases to 40 m/s compared to 45 m/s with 40 Hz. This indicates that as frequency increases the array approaches a steady actuation, such as in Figure 22. Other studies have used gate valves at each jet outlet to reduce RC, however that is not possible in this case as the fluidic oscillator chamber inherently contains capacitance. This is a limitation of the current gating method, and should be considered when interpreting the frequency response data. The peak velocity is also higher during gating at a given flow rate, which should also be considered when interpreting results.

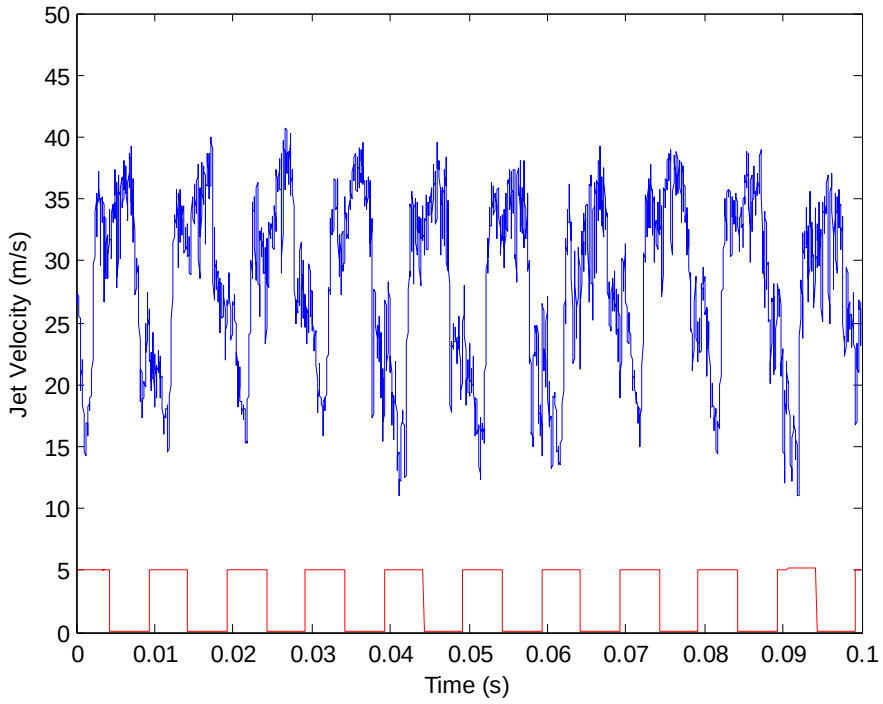

Figure 24: Gated array jet velocity, 100 Hz, 50% Duty Cycle, ~35 L/min average flow rate.

The momentum coefficient, C_μ, can give a measure of actuator power consumption, defined in Eq. 5.[9] This is the quantity that is generally quoted to measure actuator energy consumption. Subscript j indicates quantities related to the actuator jet. The area term in the denominator is selected as the model frontal area (0.078 m^2), which is done in other studies.[9]

$$C_\mu = \frac{\rho_j A_j V_j^2}{\frac{1}{2}\rho_\infty A V_\infty^2} \qquad (5)$$

The numerator represents momentum flux leaving the actuator. This quantity is typically calculated using the area and jet velocity found with hotwire data. This is more difficult with the current setup for two reasons. The first reason is that the instantaneous velocity is constantly changing due to sweeping of the oscillator and in some cases pulsing with a solenoid. The other issue is that the jet outlet is recessed, as seen in Figure 2, which prevents the exact jet outlet velocity from being easily measured. In steady (non-gated) cases, the exit velocity is assumed to be the maximum velocity measured with hotwire 4 mm from the outlet. In pulsed cases, the average velocity over several pulse cycles is used for the C_μ calculation. The minimum area of the jet outlet ($2\ mm \times 2\ mm$) multiplied by the number of oscillators in the array, n, is selected for the A_j term. The air density in the jet is assumed the same as ambient. Eq. 5 is simplified to Eq.6 with these assumptions, which likely underestimate C_μ. A more sophisticated hot wire setup could be used in the future to gain a better estimate of velocity at the outlet.

$$C_\mu = 1.03 \times 10^{-4}\ \mathrm{n}\ \left(\frac{V_j}{V_\infty}\right)^2 \qquad (6)$$

Additional hotwire data related to the actuators is found in the Appendix.

Wind Tunnel

The wind tunnel is an Eiffel type open loop tunnel that circulates air from outside of the building and is capable of 45m/s test section airspeed. The test section dimensions are 39" tall, 55 " wide and 96" in the streamwise direction. The turbulence intensity was previously measured as 0.55% in the center of the test section, which is assumed with quiescent conditions at the inlet. Additional low frequency turbulence is expected in the current study due to wind gusts at the tunnel inlet and outlet. The model is placed in the center of the tunnel, with the edge of the model 54 mm from the edge of the tunnel closest to the window. The front model feet are placed on the boundary between the wooden and acrylic floor sections, Figure 20. The model is secured with chains attached to the front feet and secured through the tunnel floor 12" ahead of the model. The model pitch and yaw angles are set as close to zero as possible.

Drag Force Measurement:

The drag force is measured using a load cell that is built into the model. The load cell is capable of measuring force on a single axis in the direction parallel to the length of the model, which is the definition of drag in this case. The measurement system uses a linear stage to allow the body of the model to slide relative to the supports with very low friction, Figure 25. The feet of the model are connected to a frame inside of the model that is attached to the top of the linear stage. The body of the model is connected to the lower side of the stage. As the body of the model is pushed backwards a button load cell, connected to the body, contacts the frame. The load cell accepts the drag force $\pm$ friction from the linear stage.

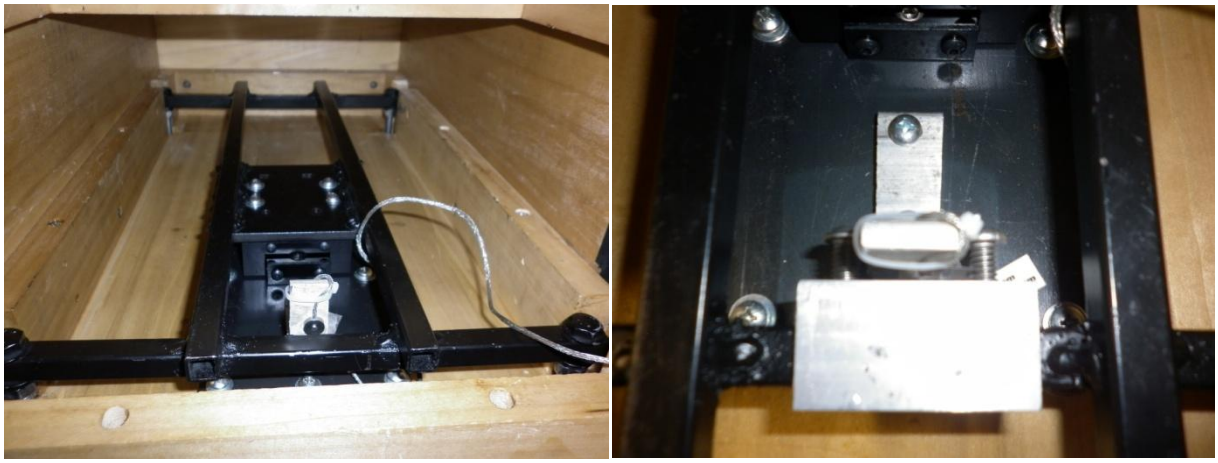

Figure 25: Load cell system, linear stage allows motion between supports and model. Drag force from model is transmitted to the button load cell and then to the support frame.

The load cell, OMEGA LCKD-10, is supplied with 5.0V DC and a voltage signal proportional to the applied force is output. The load cell was initially selected to maximize accuracy in the 0-10 lb range, which is the range expected for the initial test plan. The test plan was later changed to a lower tunnel speed, which would have allowed a 5 lb range load cell. The total uncertainty associated with the load cell is stated as 0.5% FSO, which is roughly 1.5% the measured drag force. Note that the total uncertainty of the measurement system is higher due to friction in the linear slide, which leads to hysteresis. The raw voltage signal from the load cell is sent to a filter amplifier with an input gain of 30 dB and low pass cutoff of 15 Hz. This results in a measured voltage ranging from 10 mV to 150 mV. This signal is read into LabView using a PCI interface. The tunnel speed is also read into the same program to allow for greater accuracy in the calculation of the drag coefficient.

The measurement system is calibrated after each test configuration is changed. The difference in weight between the test setups will result in a different zero drag offset measured at the load cell. This is because the tunnel floor is not perfectly perpendicular to the direction of

gravity. The nose of the model is effectively higher than the rear, which causes a portion of the model weight to be measured as drag, so the zero force offset must be found during calibration. This concern would be eliminated in more sophisticated six component load cell, which was not within budget. The calibration procedure measures the voltage from the load cell at 0,1,3,5,3,1,0 lbs. to determine any hysteresis effect. The calibration force is applied using a weight and pulley system, Figure 26a. The friction in the pulleys and the weight of the connector are considered to be negligible. An example calibration measurement is shown in Figure 26b, which is fit to a first order polynomial in MATLAB to later convert voltage to force. This indicates that a hysteresis error of 5% is present in the measurement system. This brings the total uncertainty of the drag measurement to 6%.

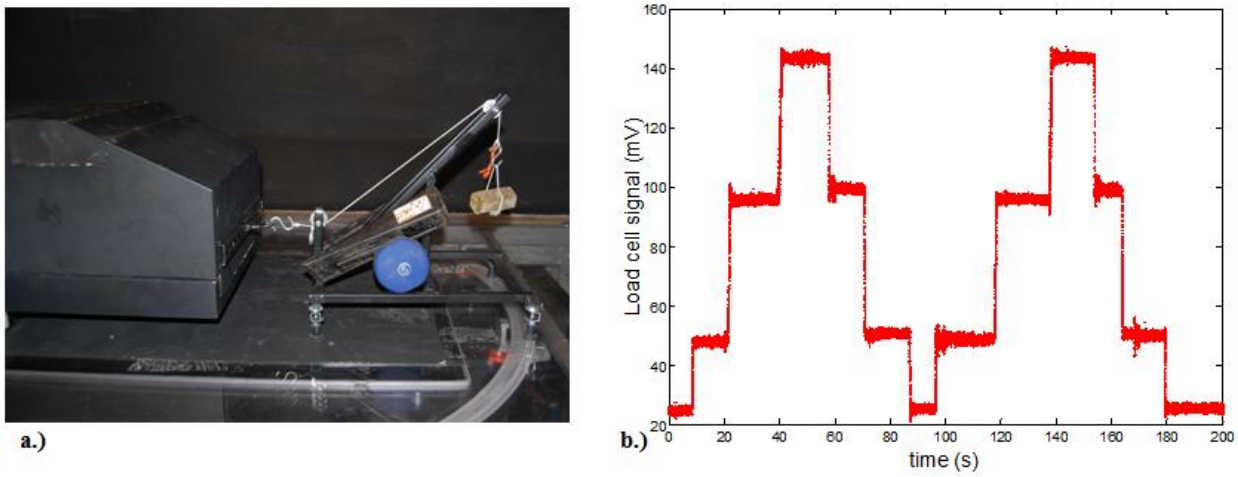

Figure 26: Calibration setup **a** and measured voltage during the calibration process **b**.

Smaller changes in force than predicted with the static calibration analysis can be measured by the system in practice. This is thought to be due to vibrations of the model that constantly change the direction of friction, which is the main source of hysteresis error in this system, and also may keep friction in a constant state of sliding friction, which is generally less

that static friction. The system has been observed to measure changes in drag less than 2% with high repeatability.

At high tunnel speeds, the vibration of the model increases and this may have an adverse affect on the measurement system. Figure 27 shows a plot of the drag signal as a function of airspeed. Notice the increase in deviation from the mean as the velocity and vibration increases. This may lead to higher than actual measured drag at high airspeeds. This is inferred by the increase of measured drag coefficient with Re which is the opposite trend than other studies have seen. A possible improvement to the measurement system may be to preload the system with a spring to reduce vibration amplitude. This effect is of little concern at the flow speeds used in the current study.

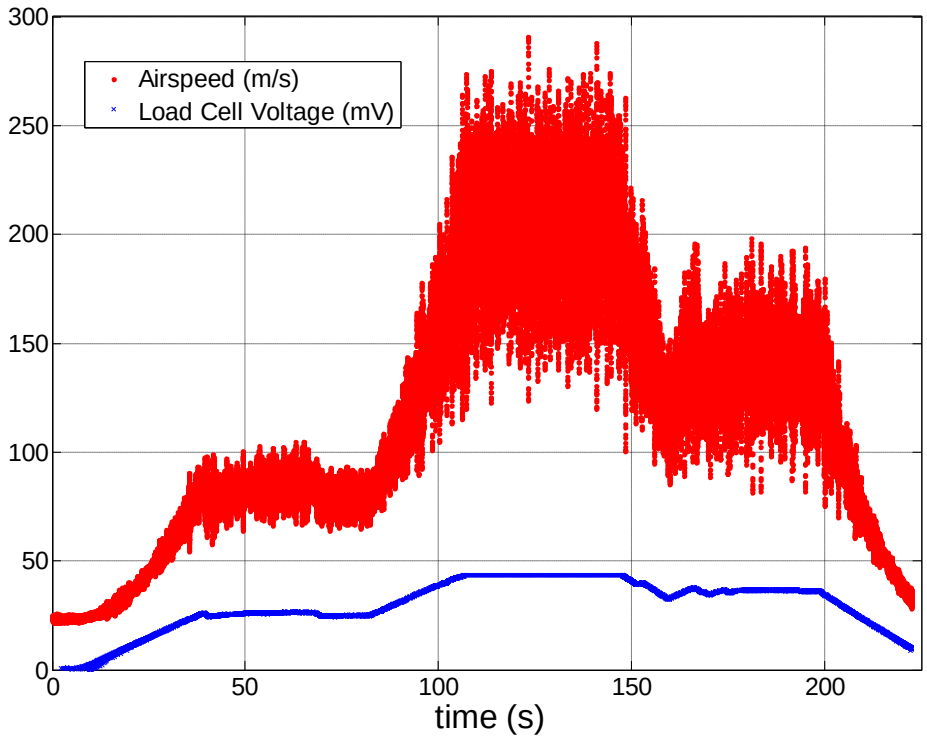

Figure 27: Drag measurement signal as a function of time and airspeed.

The load cell cable and air lines are routed through a hole in the model and through the wind tunnel floor. There is concern that the physical connections between the model and the surroundings will result in measurement error. For example, the hose may pull on the model and result in a drag reading that is artificially high or low. This concern, while difficult to eliminate, is reduced by creating a slot in the wind tunnel floor to allow the hose to slide freely beneath the model.

Another source of inaccuracy in the drag calculation is from the thrust generated by the actuator jets. This type of force, although generally small, should be subtracted from the drag measurement calculation for and accurate measure of the affect flow field change has on drag. The thrust force is measured in quiescent conditions, using the calibration setup. The thrust component is estimated by hanging a one pound weight to the calibration balance and activating the jets. The jets reduce the amount of the force measured at the load cell, and thrust is then calculated from the difference in force. This force is generally negligible with the present actuator flow rates.

Imaging and Flow Visualization

Different imaging techniques are used to gain a qualitative and quantitative understanding of the flow field, which is invisible without such methods. One technique is smoke visualization, which uses smoke to reveal the flow patterns. A smoke generator is placed at a particular location in the wind tunnel entrance such that the stream reaches the intended location on the model. This powerful technique allows a quick assessment of the flow field.

Other techniques are used to indicate the direction of flow near the surface. One technique is tuft visualization, which uses pieces are yarn taped to the surface of the model. This

method can quickly indicate features such as flow detachment, vortices, and recirculation. Another related method uses oil mixed with pigment on the surface of the model to indicate the flow direction near the surface. This technique is valuable because it give a continuous map of the surface flow pattern, compared to the discrete locations with the tuft. Oil flow gives a time-averaged representation, while the tufts can illustrate unsteadiness. There are advantages to each method so both are attempted.

A more involved technique called particle image velocimetry-PIV is used to quantitatively map the velocity field in a selected plane. PIV uses a laser and high-speed camera to capture the location of seed particles immediately before and after a short time interval, in this case 100 μs. The seed particles' locations will change slightly between the two frames. From the raw images, the human mind can see the flow field by quickly toggling the two images. To gain a quantitative understanding, a computer program is used to map and correlate individual particles between frames and from this, a velocity field is computed. The vector fields from each image pair sometimes do not contain a complete vector field due to improper seeding or inability to correlate particular for a particular segment of the image. Also, due to the unsteady nature of the flow, a single image pair may not fully represent what is happening on average. For example, the single pair may capture the vortex at one extreme of the shedding cycle. The transient processes are important to understand, however for this study only the average field will be examined. To accomplish this many image pairs are taken, the vector field computed, and then averaged in order to find a complete vector field of the flow.

The PIV setup uses a YAG 532 nm double pulse laser to create a light sheet over the rear slant in the streamwise direction, which allows the wake to be imaged. Images are captured with a high-speed camera, with a resolution of 1200 by 1600 pixels, connected to a computer using

DaVis software. The camera and laser are synchronized with a timing box. The Δt value for this study is selected as 100μs to allow the maximum particle displacement to be around 5 pixels. 695 image pairs are taken and the vector field averaged for each flow field analyzed with PIV. The images are correlated using a 64 by 64 pixel decreasing window with 50% overlap. A sliding background filter option is selected within Davis to reduce the effect of systematic distortions, due to window glare and uneven laser sheet intensity, on the computed vector field. The images are then plotted in Techplot.

The flow is seeded with olive oil using an air driven atomizer at the tunnel inlet. The open loop tunnel creates difficulties with seeding. In this case the PIV images are taken at a tunnel speed of 10 m/s due to the low output from the seeder. A higher output smoke generator was also attempted, however the condensed glycerin vapor results in plumes instead of individual particles large enough to be resolved by the camera. Future seeding efforts in the tunnel should use multiple atomizer type seeders at several locations in the inlet. Consideration should also be taken to plan PIV runs when the temperature is above the solidification point of olive oil or use a different fluid. In this case, a heater was used to keep the olive oil from freezing.

The PIV setup is shown in Figure 28. The camera is positioned approximately 1.5 m from the image plane. The laser is placed above the tunnel and the beam is reflected to a cylindrical lens, which creates a sheet that shines on the area of interest. In this study, all images are taken of the symmetry plane. The extent of the image plane on the model is shown in Figure 29, and is the same for each slant angle that was imaged. A high zoom lens was used to achieve this image plane. An attempt was made to create a larger image plane but the resolution of the camera is not high enough to resolve individual particles at the further distance. The system is

calibrated using a grid with known spacing that the computer uses to calculate and compensate for distortion as well as provide a distance between pixels, which is necessary to compute velocity. This calibration shows the final image plane to be about 150 mm tall and 200 mm wide. The right extreme of the plane is 180 mm from rear the model and the upper portion is 45 mm below the roof of the model.

Figure 28: PIV setup, laser placement (Left), camera placement (Right)

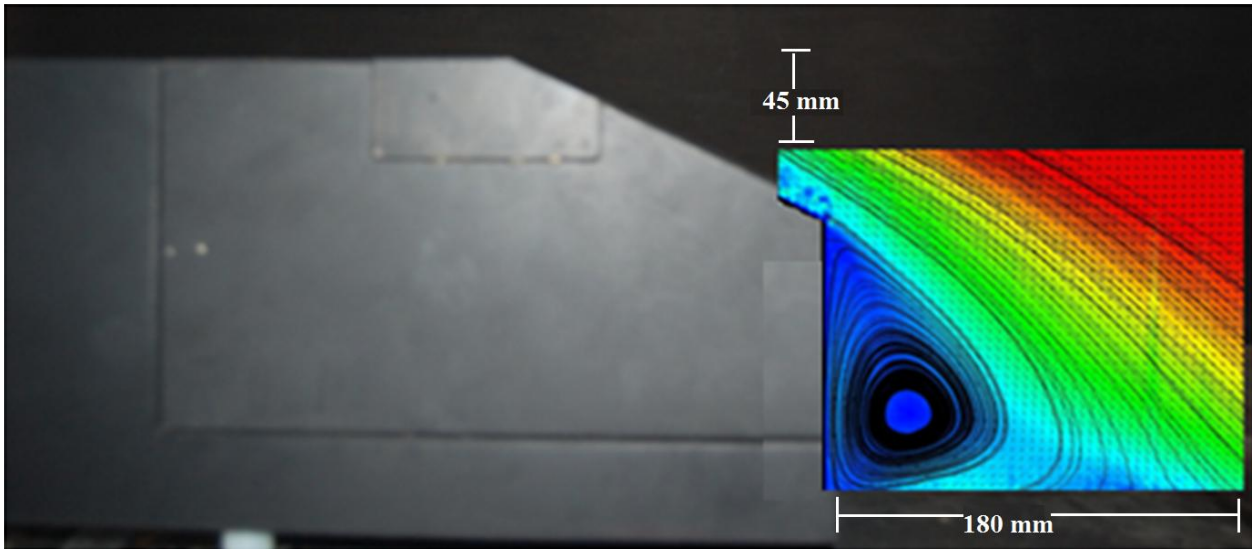

Figure 29: PIV image plane relative to the model.

Results:

Baseline

Baseline drag measurements are taken to verify the performance of the Ahmed model. The test speed used in this study is 24 m/s, which corresponds to $R_{e_L} \approx 1.4 \times 10^6$. This Re is used in other studies related to flow control on an Ahmed model, but on the lower range. This speed was selected partially because of the low flow rate capability of the solenoid valve that supplies the oscillator array. The lower flow speed increases C_μ and allows the current actuator setup to have a larger influence over the flow.

The blockage in the test section is 5.7%. This is higher than other studies, which typically have a blockage around 2-3%. The higher blockage theoretically leads to higher drag. The blockage effect can be corrected for using the MIRA area ratio method shown in Eq. 7, where E is the blockage ratio defined as the ratio of model area to test section area, which is 0.057 in this study.[4] This indicates that the open test section drag coefficient is roughly 0.90 the measured C_D. This is correction is only necessary to compare C_D to other studies, the percent change can be found without it. The correction is only used on the baseline measurements, summarized in Table 3.

$$C_D = \frac{C_{D_{measured}}}{(1+2E)} \qquad (7)$$

The baseline C_D for all slant angles is higher than seen by Ahmed. This is partially the result of the current tests being at a lower Re, 1.4 million compared to Ahmed's 4.3 million.[13] Another reason may be the result of additional instabilities created by the interface between the rear slant pieces and the model body. The 25^o case has the highest measured drag, which is

expected. The drag coefficient of the 45° slant is less than the 90° case, which does not coincide with the Ahmed results. Drag for 90° setup is 12% higher than Ahmed et al found. The reason for this may be to a difference in model ride height, which can have an effect on the resulting torus structure. The ride height relative to the overall scale of this Ahmed model is roughly 8% higher than the original study, which was done to accommodate the measurement setup. The reason for this difference in drag coefficient may be investigated later, however the qualitative flow characteristics behave as expected.

Table 3: Baseline drag coefficients at 24m/s

Slant Angle (degrees)	**25°**	**45°**	**90°**
C_D ($Re = 1.4 \times 10^6, V_\infty = 24\ m/s$)	0.33	0.29	0.32
C_D (Blockage Corrected)	0.30	0.26	0.28
C_D (Ahmed- Blockage Corrected)[9]	0.28	~ 0.25	0.25
% Difference (Ahmed and Current)	7%	~ 4%	12%

The drag coefficient as a function of Reynolds number was also examined briefly. This shows that the measured C_D generally increases as tunnel speed increases, which is not expected. Other studies have seen a decrease of 1.1% per million Re.[7] The drag increase with Re indicates a possible systematic error in the measurement system. It is possible that the recovery time of the load cell is too slow to recover from the random high frequency impacts due to model vibration, which may lead to a higher than actual average force at the load cell. An example of the measured signal during a 0-45 m/s test is shown in Figure 27. Notice that the amplitude of the noise increases tunnel speed increases. For a constant airspeed, this systematic error is not expected to have a significant effect on percent change of C_D, which is the important result. In the current study, this is not a large concern because the tunnel speed is kept at a relatively low speed of 24 m/s.

Spanwise Oscillator Array - SOA

The spanwise oscillator array was tested under steady and pulsed conditions on all three slant angles. A drag reduction up to 7% is seen on the 25^o slant while negligible change is seen on the 90^o slant. A drag increase is seen on the 45^o degree slant, possibly due to the formation of streamwise longitudinal vortices, this phenomena will be discussed further in the Coanda results section. All configurations show a response to periodic forcing.

SOA 25^o

The 25^o case naturally contains longitudinal vortices and a closed separation bubble over the rear slant. Forcing along the roof slant interface was shown to reduce drag by up to 7%, compared to the actuator off state, with steady actuation at $C_\mu = 1.1 \times 10^{-3}$, . The SOA actuator was used with jet outlet angle of 135^o relative to the model roof. Figure 31 shows the near wake with and without forcing. The PIV images are taken at 10 m/s due to limitations of the particle seeder, but the qualitative flow field changes are expected to be similar.

In the forced condition, the upper recirculation core is 45 mm further from the model than in the unforced case. Moving the upper vortex core further from the base increases pressure on the vertical surface below the slant, which reduces drag.[3] Figure 31 shows that the velocity above the slant end is higher and the trajectory off of the slant is shallower in the actuated case, indicating a decrease in the separation bubble. Reducing the separation bubble has been associated with increased pressure on the slant and attenuation of vortex strength.[3] These combined changes lead to the drag decrease.

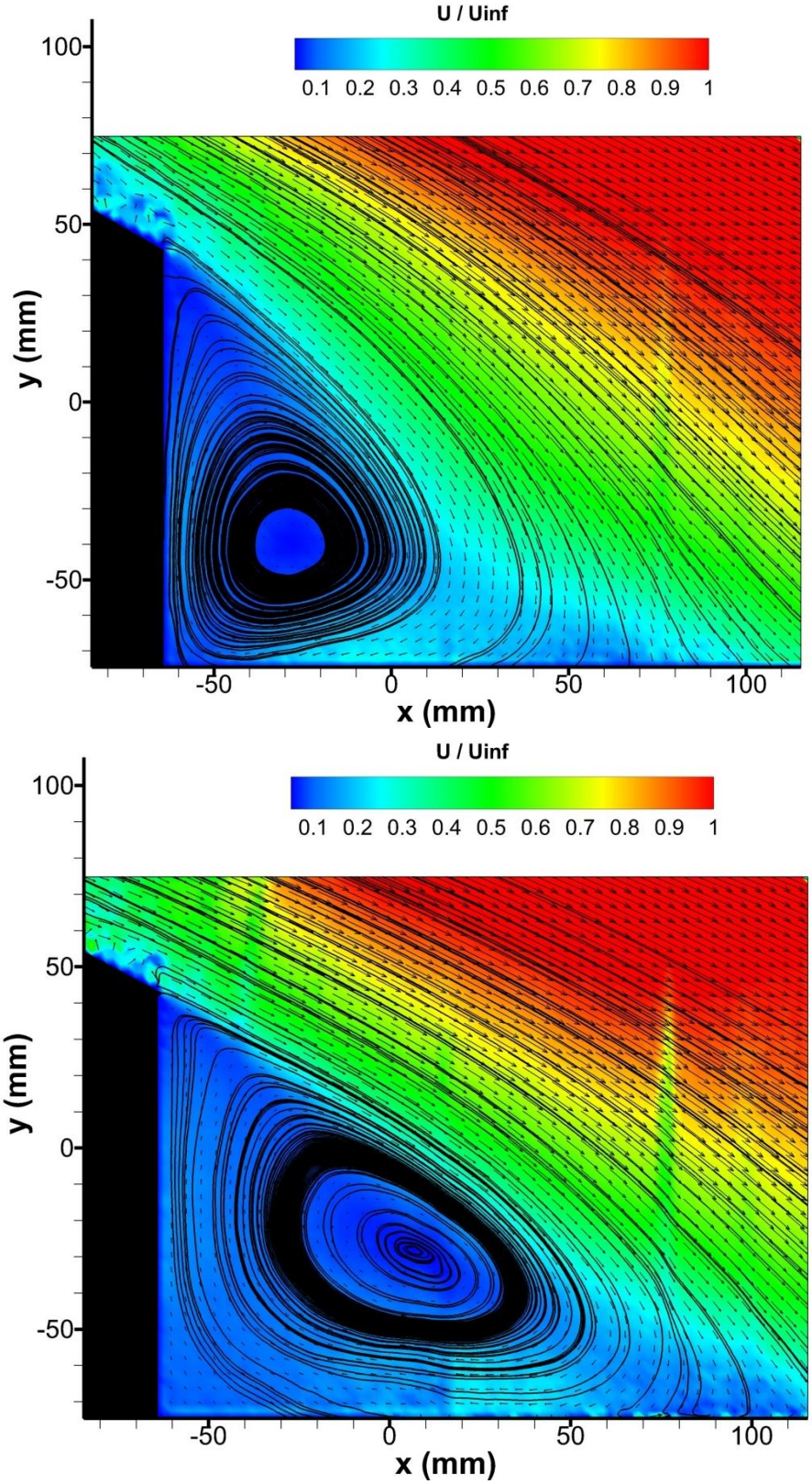

Figure 30: PIV for 25° SOA, (Upper) Actuator OFF, (Lower) Actuator ON, 10 m/s airspeed, $C_\mu = 7.0 \times 10^{-3}$.

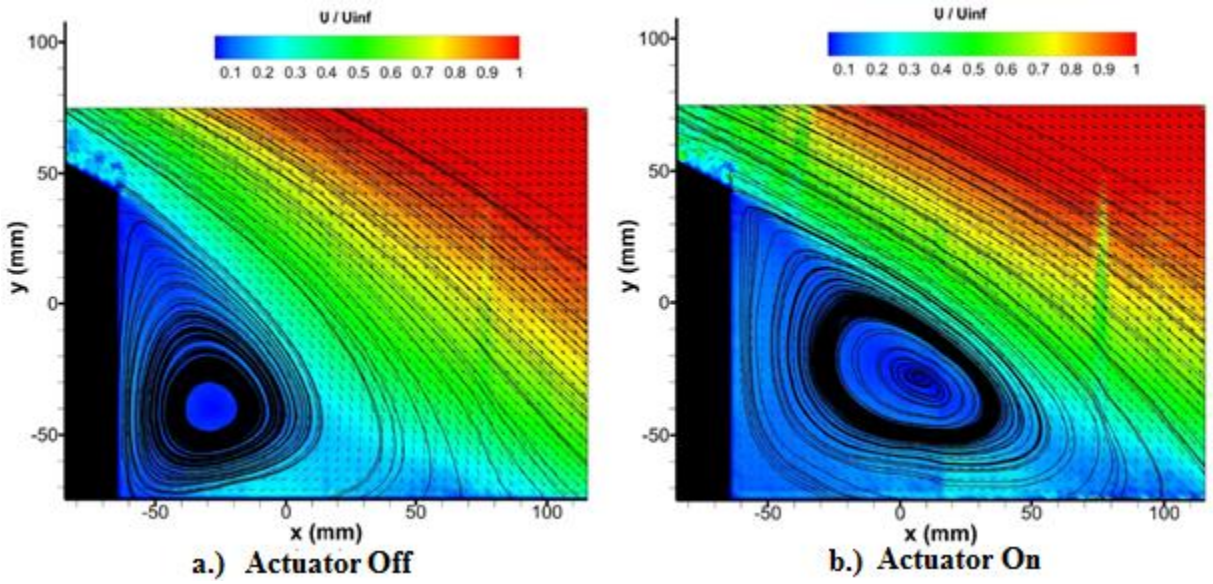

Figure 31: PIV image of 25° SOA configuration at 10m/s. **a** is baseline (off) and **b** is with steady actuation.

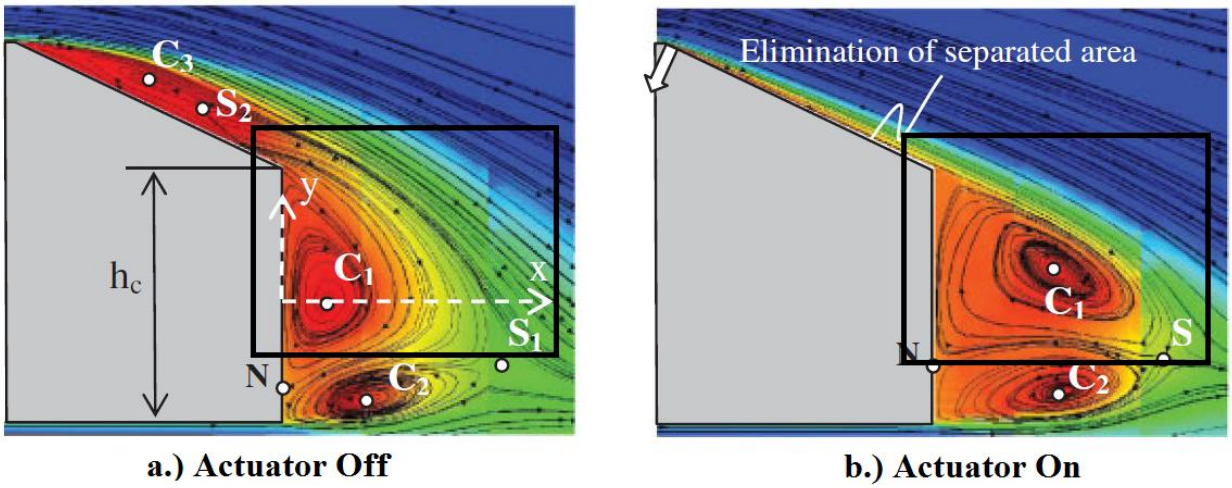

Figure 32: Results seen by Roumeas et al. using suction at the top slant edge.[3]

A study by Ruomeas et al. was able to achieve similar results using suction at the slant top edge.[3] Notice the qualitative flow field change similarity between this, Figure 32, and the current study, Figure 31, using completely different methods.

The drag coefficient was seen to vary with pulsing frequency. Frequency is measured in 5 Hz increments during a trial, with frequency always increasing. The drag coefficient is measured over a 25 second interval for each frequency level. Frequency is represented by the dimensionless Strouhal number, defined in Eq. 8, where F is the actuation frequency, h is the vertical height of the rear slant (0.077 m) and V_∞ is the far field velocity (24 m/s). This particular definition was selected to compare to the results by Joseph et al. seen in Figure 13.[16]

$$St_h \equiv \frac{Fh}{V_\infty} \qquad (8)$$

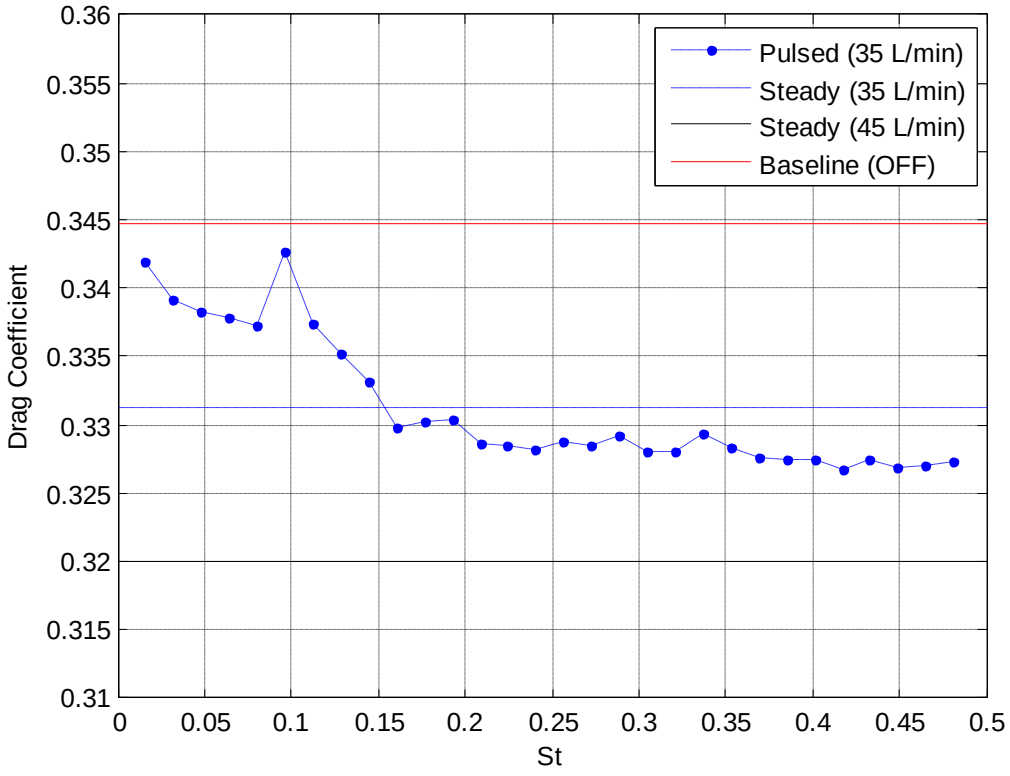

Figure 33: Pulsed SOA 25° frequency response, 50% duty cycle, 24m/s.

All of pulsed 25° SOA cases show a frequency dependent drag response, exemplified by Figure 33, which shows drag coefficient vs. Strouhal number. At low gating frequencies the drag reduction is slightly less than with steady actuation at a given flow rate, seen in Figure 33 and Figure 34. A relative spike in drag is seen at $St_h = 0.1$, which was shown by Sasaki to be associated with shear layer flapping.[16] Drag then decreases as frequency increases. The setup may possibly be approaching the drag minimum seen at $St_h = 0.6$ by Joseph, et al. This is also seen in Figure 34 and Figure 35 at average flow rates of 30 and 45 L/min respectively. This must be investigated further with flow visualization for sufficient explanation to be given.

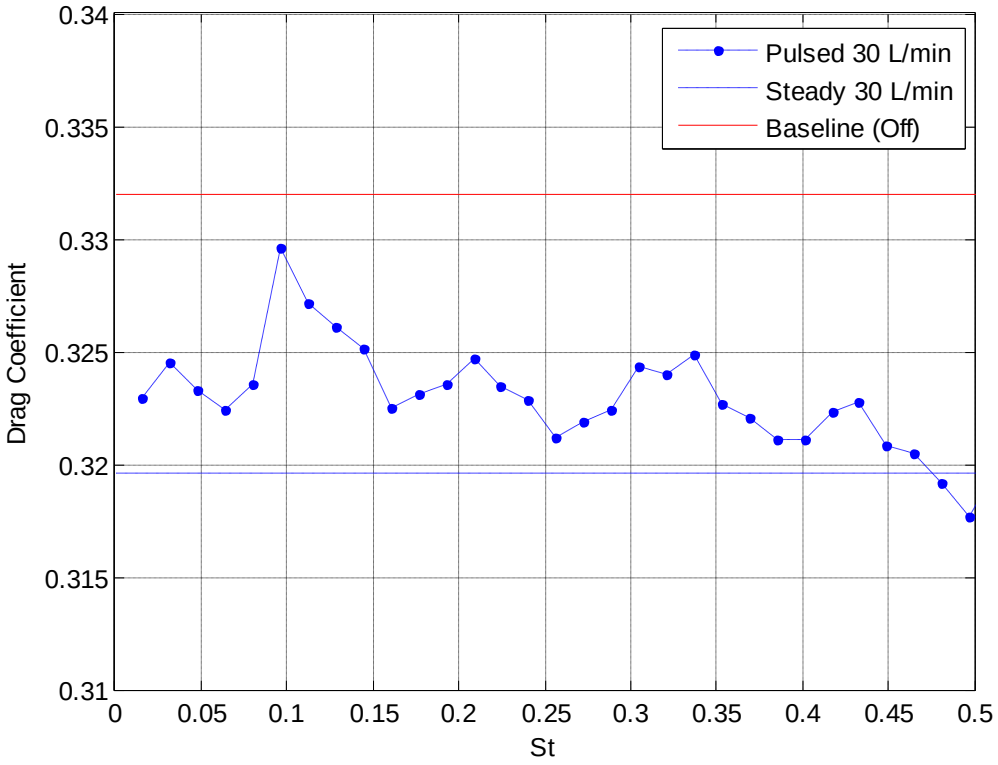

Figure 34: Pulsed SOA 25° frequency response, 30 L/min, 50% duty cycle, 24m/s.

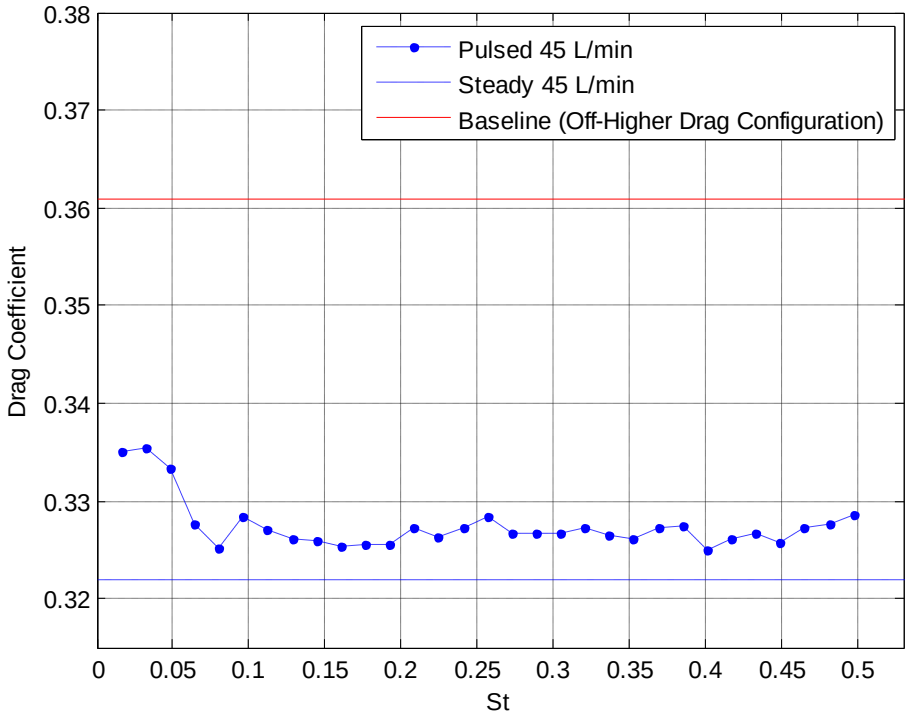

Figure 35: Pulsed SOA 25^{o} frequency response, 45 L/min, 80% duty cycle, 24m/s.

Notice the higher drag actuator off drag of 0.36 in Figure 35. This was measured before putty was added to the actuator-slant interface. The poor interface leads to a much higher drag than the modified case, however it is interesting to note that an 11% reduction is seen over the actuator off case with a 45 L /min actuation case.

The maximum reduction of 7% is seen with steady actuation at $C_\mu = 1.1 \times 10^{-3}$, Figure 33. This C_μ is less than half of what Joseph et. al required for a similar reduction with actuation at the slant top, Figure 13b. This is promising as it suggests that fluidic oscillators have the potential to reduce actuation energy needed for a given drag reduction.

SOA 45°

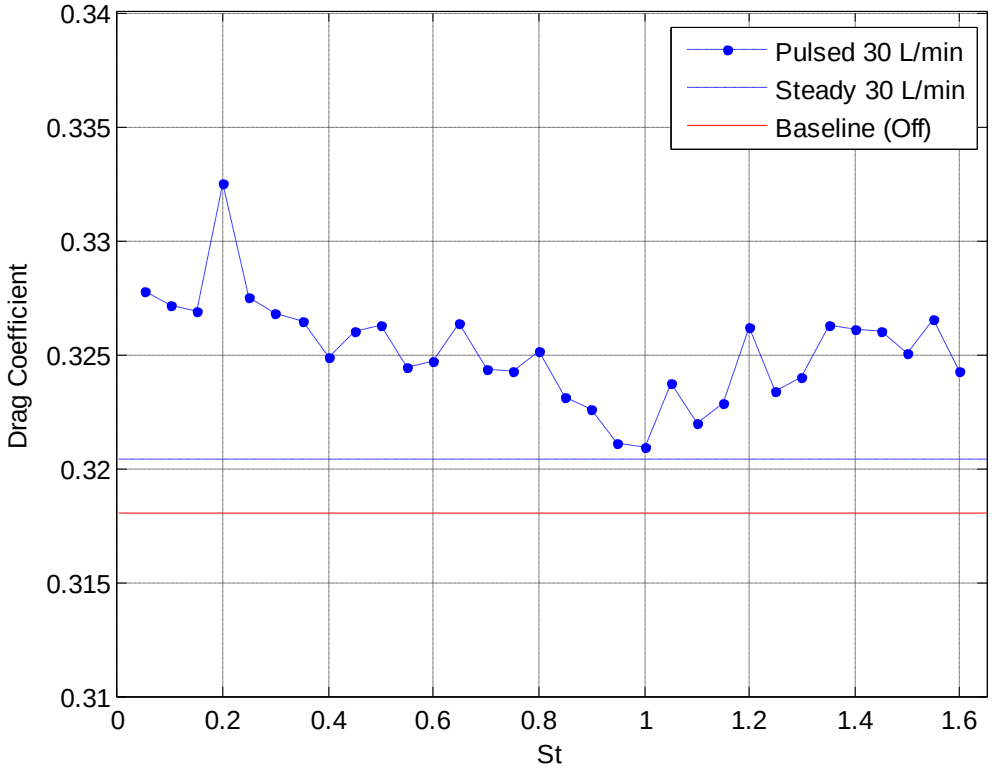

Figure 36: Pulsed SOA 45°, 30 L/min, 50% duty cycle, 24m/s.

The Strouhal number is defined with a different length scale for the 45° SOA case, where H is the model height (0.239 m), to allow comparison with the results of Brunn et al, Eq. 9.[9]

$$St_H \equiv \frac{FH}{V_\infty} \qquad (9)$$

A drag increase is seen with both steady and pulsed excitation and a jet exit angle normal to the slant at the interface of the roof and slant surfaces. A greater increase is seen with pulsed excitation. The drag spike at $St_H = 0.2$ coincides with natural vortex shedding and seen as the most efficient frequency by Brunn in their original 2-D study.[9] In that study a 27% drag reduction was witnessed and a large flow field change associated with attachment was seen, Figure 11.[9] It was later learned that the principles were applied by the same researchers to a 3-D

Ahmed model in a wind tunnel and a drag increase was witnessed due to the formation of longitudinal vortex structures.[17] The structures, which cannot form in the 2-D study, lead to the drag increase in the 3-D problem. This suggests that control of the vortices that form during attachment must be controlled for a drag decrease to be seen on this setup.

SOA 90°

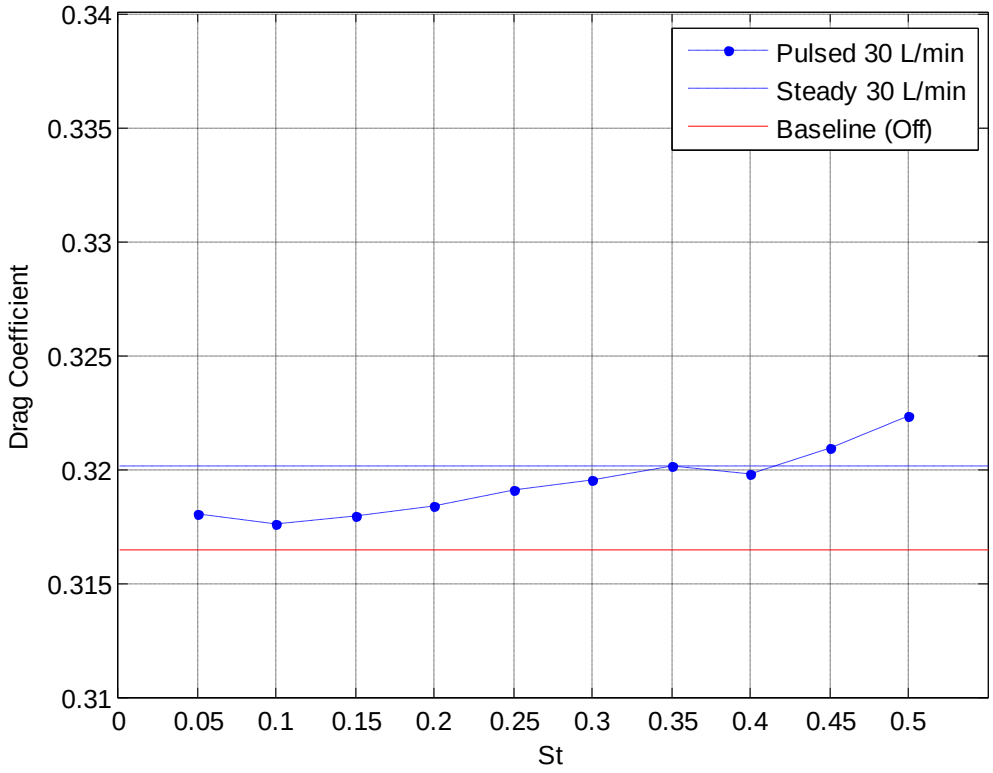

Figure 37: Pulsed SOA 90°, 30 L/min, 50% duty cycle, 24m/s.

The results from the 90° SOA are less clear than on the other slant angles. There appears to be a frequency dependent drag increase, Figure 37, which shows the result with actuation at roof end, with angle of 120° relative to the roof. It is possible that the array may be introducing stream wise instabilities created by interactions between oscillator jets, which could lead to

increased drag. It is also possible that the spanwise vortices from the top and the bottom of the model are interacting unfavorably.

In another study that attempts periodic excitation on a square back model, similar to the Ahmed body, control used on the roof and also on what corresponds to the underside of the vehicle to match the phase of upper and lower vortices and increase the base pressure.[18] This was an effective 2-D study, with the model spanning the width of the tunnel, and placed in the center of the tunnel create symmetric flow across the top and bottom of the model so this and the current case are not precise analogues.[18] This may illustrate the need to control shedding from the top and bottom of the model.

Coanda Results

The Coanda surfaces were shown to have a profound effect on the wake on both the 45^o and 90^o cases, however a drag increase is experienced. As with the SOA 45^o case, the formation of longitudinal vortices is suspected to contribute to this increase. The 25^o case sees a slight reduction over the actuator off case.

Coanda 25^o

The drag coefficient for the 25^o slant as a function of actuation flow rate is shown in Figure 38. A maximum drag reduction of 3% is seen at a flow rate of 60 L/min, corresponding to a jet velocity of 29 m/s and ($C_\mu = 1.4 \times 10^{-3}$). This is likely the result of a reduction in the closed recirculation bubble. A possible drag increase is seen at a flow rate of 20 L/min, however this may be within the margin of measurement uncertainty. The higher C_μ makes this less favorable than the SOA case.

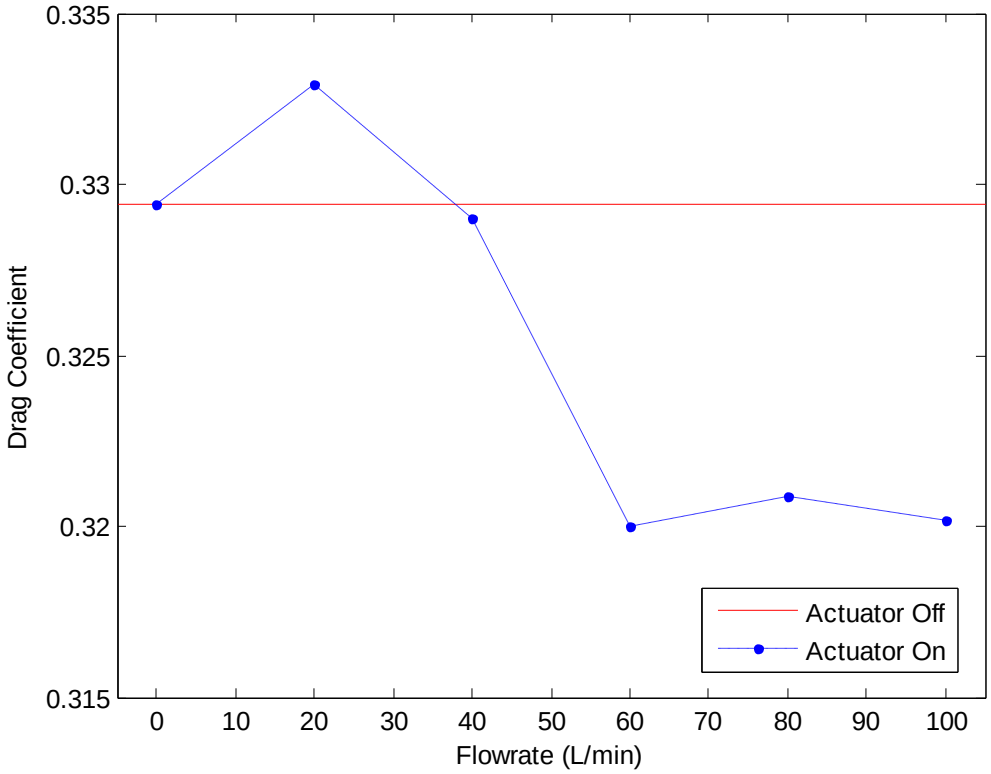

Figure 38: Coanda 25^{o} drag as a function of flow rate.

Coanda 45^{o}

One of the most profound results of this study is seen on the 45^{o} Coanda configuration. The baseline flow is fully detached, Figure 39 and Figure 41. Notice the low velocity recirculation region which rotates clockwise in Figure 41. As the actuators are turned on the flow attaches to the slant, Figure 40 and Figure 42, indicated by a velocity close to freestream near the surface. This is associated with a drag increase. It is expected that attached flow will result in pressure recovery on the slant, however this benefit is reduced for several reasons. One reason is suction on the Coanda surface, which results in a locally low pressure and is used to attach the flow. Another reason it that this local decrease in pressure used to attach the flow is not offset with a stagnation region on the back of the model. Notice how the flow from the top

of the model leaves the slant and attaches to the floor. A better design would include control on the underside to have this flow meet the flow from the slant somewhere on the back of the model. This is difficult to accomplish without a moving floor, which keeps the flow under the vehicle at a high velocity and simulates the condition seen by real vehicles.

Figure 39: Coanda 45^{o} smoke visualization, actuators off, 10 m/s.

Figure 40: Coanda 45^{o}, actuators on, 10m/s.

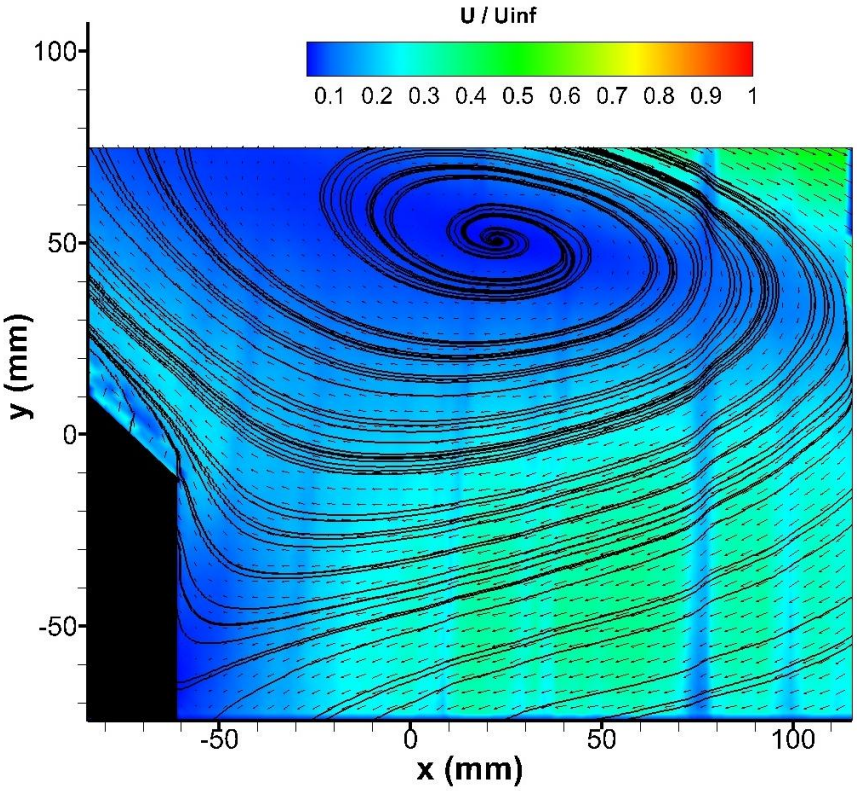

Figure 41: PIV 45^{o} actuators off, 10m/s .

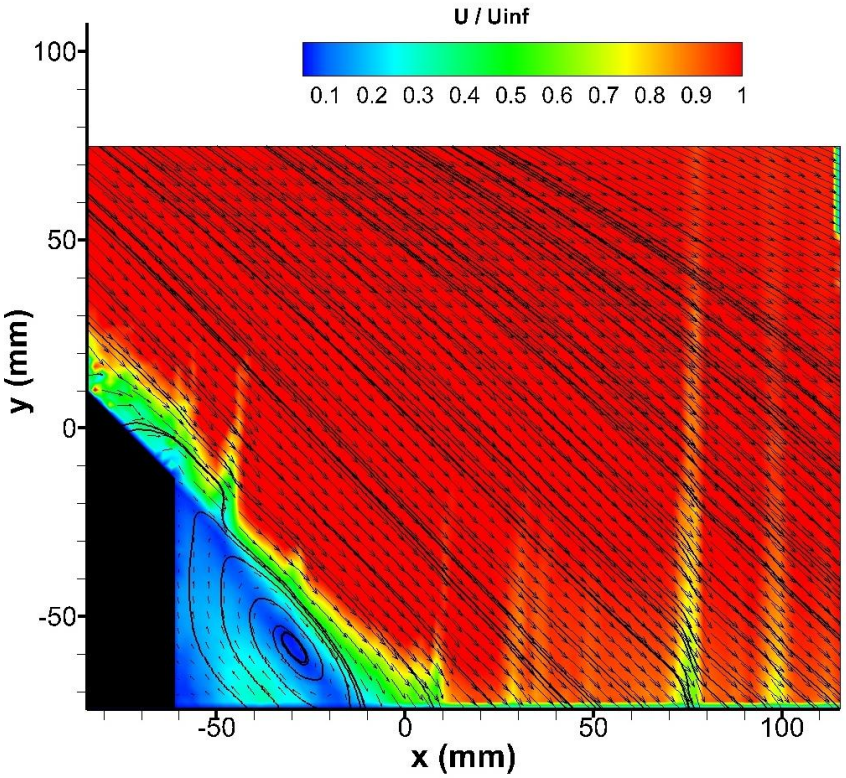

Figure 42: PIV 45^{o} actuators on, 10m/s.

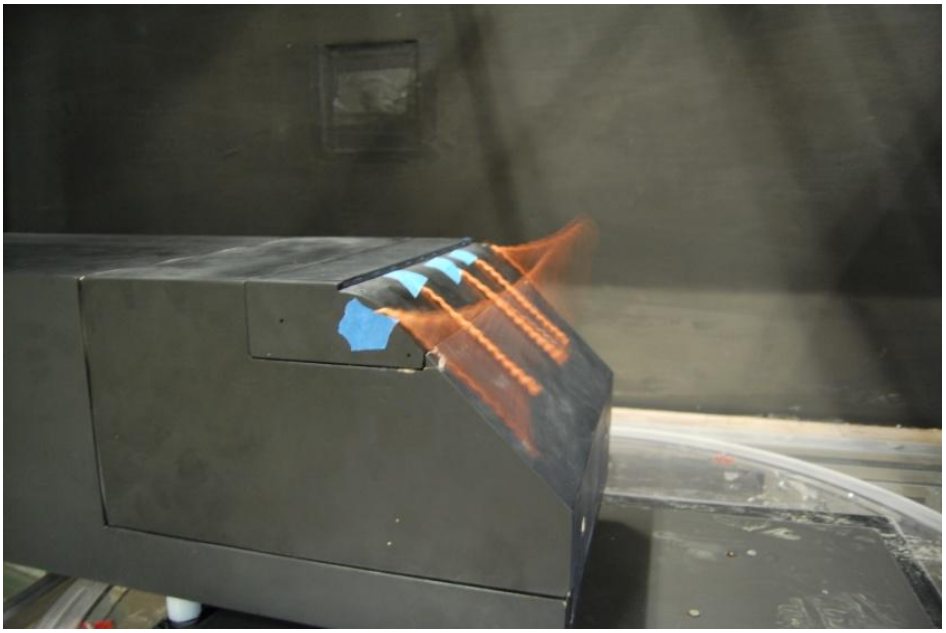

Figure 43: Longitudinal vortices on the Coanda 45^{o} configuration.

The most significant reason for the drag increase may be due to longitudinal vortices that form on the slant, seen in Figure 43. This is a similar effect seen by Brunn et al. and is thought to also be the reason for drag increase on the 45^{o} SOA. Attachment allows vortices to form in the region that was previously dominated by reverse flow on the slant, when the actuators were off. Another reason for the strength of the vortices may be due to the strong low pressure region on the Coanda surface, which causes flow from the sides to roll up into a vortex. Pressure taps should be used to verify the relative contributions of each of the reasons mentioned. The results reiterate that this 3-D problem requires multiple control solutions, vortex and separation control, simultaneously. This degree of control seen in the images is at a relatively high flow rate of 100 L/m at 10m/s tunnel speed, which corresponds to a relatively high $C_{\mu} = 18 \times 10^{-3}$.

Coanda 90°

The Coanda surfaces and fluidic oscillators were also able to significantly alter the flow on the 90° slant. The baseline PIV image is shown in Figure 44, at the same location as Figure 29, which corresponds the vertical center of the of the model. Two spanwise vortex cores exist beyond the upper and lower extremes of the image. High actuator flow rates are needed for an attachment response. Figure 45 shows the result of actuation at a flow rate of 100 L/min with an airspeed of 10 m/s, $C_\mu = 18 \times 10^{-3}$. Notice how the upper vortex core, which was previously out of the image plane, is shifted downwards and towards the model. The lower right quarter of the image is distorted due to insufficient seed particle density.

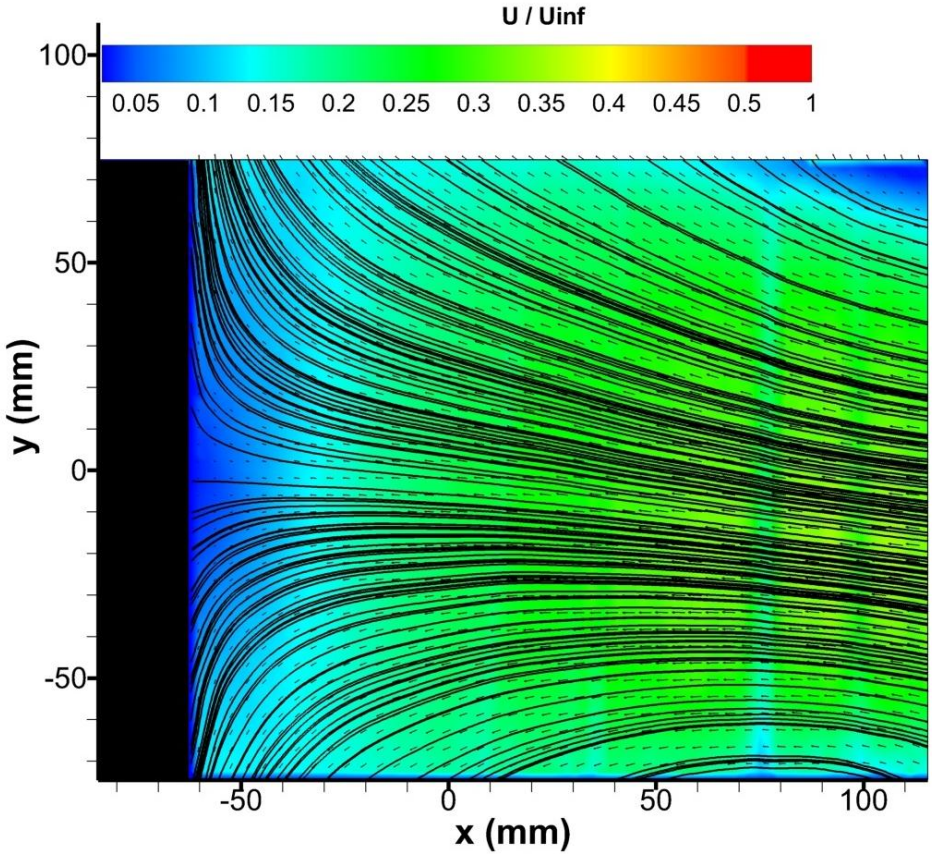

Figure 44: Baseline flow Coanda 90°, 10m/s.

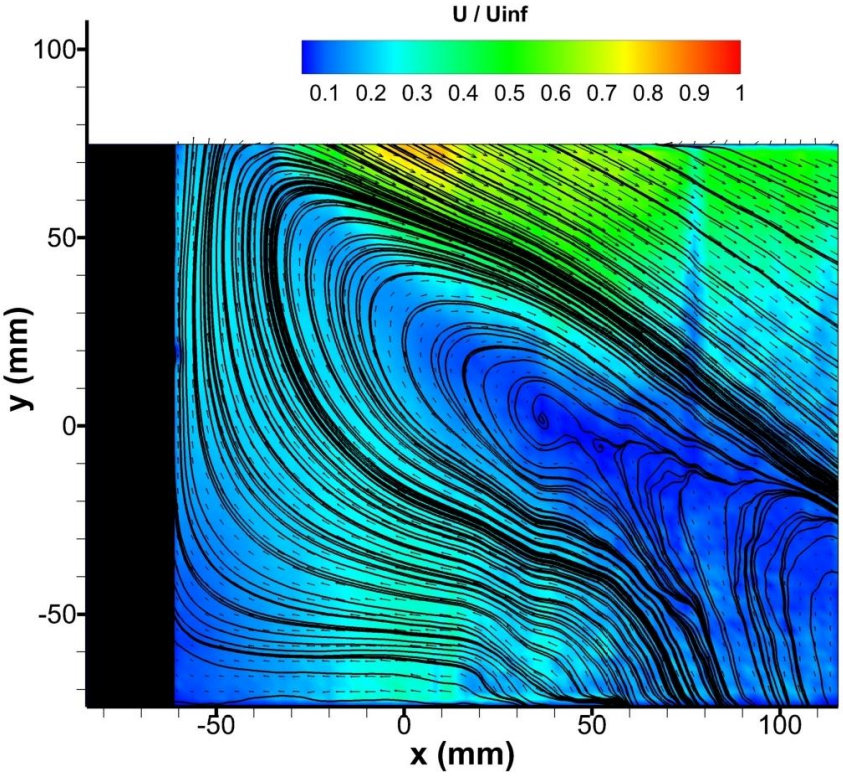

Figure 45: Actuated flow Coanda 90^{o}, 100L/min, 10m/s.

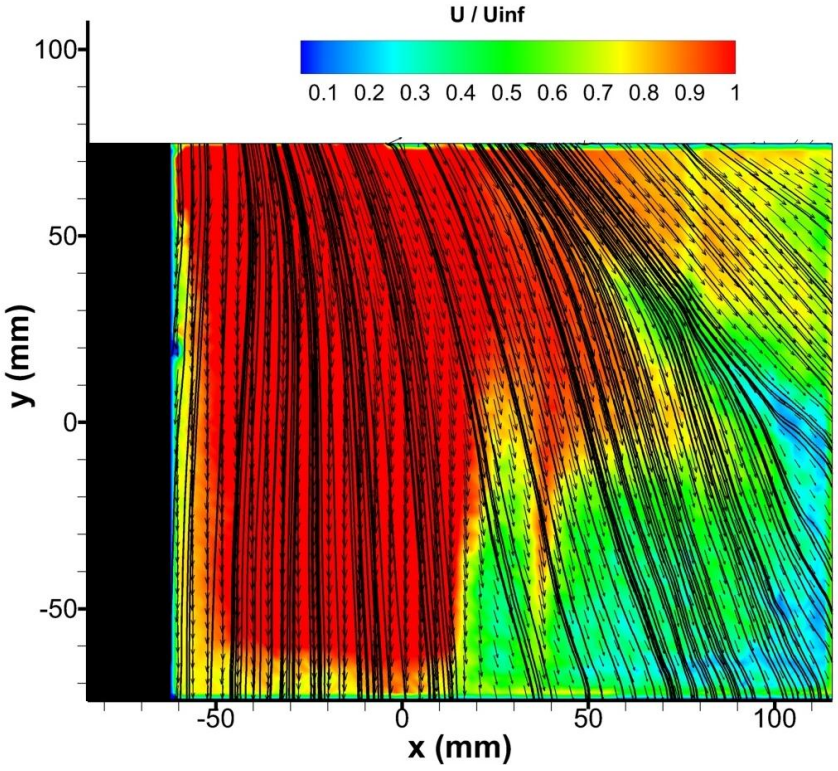

Figure 46: Actuated flow Coanda 90^{o}, ~200 L/min, 10m/s.

Figure 46 shows the result at a flow rate goes beyond the meter capability but is estimated to be around 200 L/min based on the audible frequency change of the oscillators. This shows a significant degree of attachment to the vertical surface and an elimination of the upper recirculation region. Both of these cases result in drag increases for similar reasons as the 45^o Coanda case. Vortices are observed to form on the Coanda surface even on the 90^o case.

The Coanda surfaces illustrate that attachment can be achieved on the high angle configurations, however with a relatively high actuation flow rate, which was expected. What was unexpected is the drag increase seen with attachment, possibly due to vortex longitudinal formation. This indicates the need for separation and vortex control simultaneously.

Other Configurations

Other experimental configurations were also tested, however to a lesser extent due to time constraints. One of these involved oscillators with jet sweeping oriented parallel to the flow. This setup is termed the "Periodic" configuration. The goal is to have the oscillator jet continuously induce vortex formation from the shear through the entire sweeping cycle. The main issue with this setup is that the jets do not move synchronously. The phase is random between oscillators so a coherent spanwise vortex may not form. This setup requires further research to synchronize oscillations.

An attempt at vortex control on the 25^o slant was also examined briefly with leftover parts. Fluidic oscillators were imbedded into the slant insert with the jet outlet 9 mm from the side edges. This did appear to result in significant alteration of vortices, indicated with tuft visualization, at the flow rates that were examined. This may require another custom design that embeds the oscillators closer to the edge, where the vortices begin to form.

Conclusions:

Contributions

A drag decrease up to 7% was witnessed on the 25^o Ahmed body model using a steady oscillator array. The reduction is thought to be result of decreasing the size of the closed separation bubble on the rear slant, which also has the effect of reducing the vortex strength and moving the recirculation torus further from the model base. The C_μ required for this reduction using the oscillator array is potentially half of what a related study required for a similar drag reduction, indicating merit to the use of fluidic oscillators for vehicle flow control.[10] The drag reduction results that have been achieved using the SOA can potentially be applied to some ground vehicle applications that contain a significant closed recirculation bubble, such as that seen on the 25^o Ahmed body. The flow around real vehicles is more complicated, so the actual implications are unknown. Also at higher Re, which is an order of magnitude greater on real vehicles, the size of this circulation bubble naturally decreases so the drag reduction benefit may be less.

A strong response is seen using the Coanda surfaces with fluidic oscillators. Flow is seen to become attached to the 45^o and even the 90^o slant angle at high actuator flow rates, $C_\mu = 18 \times 10^{-3}$. Attachment results in the formation of longitudinal vortices, which are thought to be responsible for a drag increase on the Coanda configurations.

A similar but less profound drag increase is seen using the spanwise oscillator array on the 45^o angle. This result mirrors what was seen by Brunn et al. and further emphasizes the need for a holistic approach to control flow on the high angle Ahmed body and ultimately production

vehicle configurations. It may be necessary to implement vortex control in conjunction with separation control in order to for a net increase in base pressure to be achieved.

Additional Applications

The Coanda results on the high angle configurations suggest a possible use for fluidic oscillators on airfoils. The degree of attachment to the slant seen with the actuators on was notable. This type of setup, corresponding to tangential blowing on the airfoil, may be used to mitigate stall. Raghu suggests a possible implementation into the airfoil.[15]

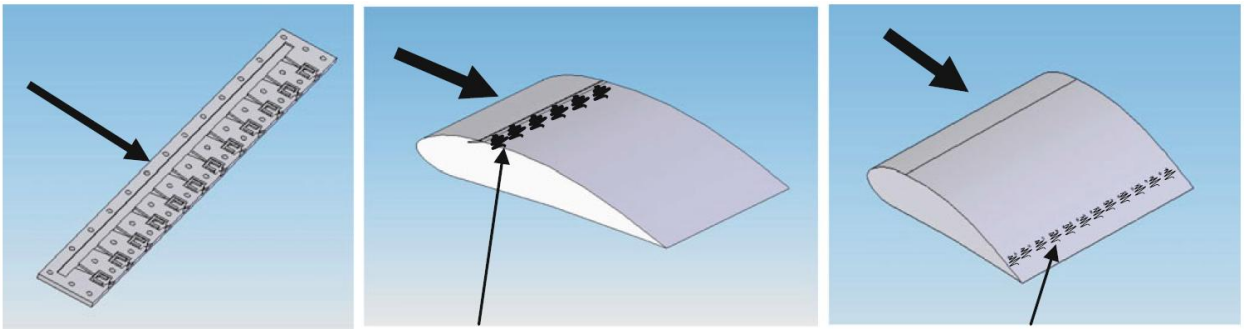

Figure 47: Fluidic oscillator array on an airfoil.[15]

This may require too large of a flow rate for continuous operation, however it could be used intermittently, powered by onboard pressurized tanks that are slowly refilled with engine bleed air. For example, if stall is detected the array of actuators may immediately be activated to reattach flow and allow time for the situation to be corrected. This could also be used in takeoff and landing situations, similar to blown flap configurations seen on some aircraft, to reduce takeoff and approach speed and allow for decreased runway length.

Future Work and Improvements:

There is much that can be built upon this research. This was a new project and much of the time was spend building the experimental setup. Near term study will further examine the mechanisms behind the frequency response at $St_h = 0.1$ on the 25^o slant and $St_H = 0.2$ on the 45^o slant. This will include a tighter frequency sweep, instead of the 5 Hz increments done in this study. It will also include flow visualization techniques such as smoke visualization or PIV at these specific frequencies. At the time PIV was taken in the current study, the data related to frequency response was not available and due to time constraints only a few of the cases could be imaged. Analysis of the pressure distribution on the slant surface may also be done with pressure taps to determine the spatial affect actuation has on base pressure.

A longer-term study will examine ways to improve upon the high angle configurations with vortex control. This may be essential for progress on these configurations. Initially this could consist of measuring the change in drag if a passive device, such as a fence at the top sides of the slant, is used to prevent formation of vortices while separation is controlled with the Coanda surface and oscillators. If a major benefit is seen, eventually active methods will be examined to specifically control vortices. This could include strategically placed oscillator arrays on the slant side edges to prevent vortices from forming. A further improvement to the Coanda surface may include control of the underbelly flow to help create a stagnation region on the rear of the model, which should further increase base pressure, as opposed to having the flow from the slant attach to the ground. The results from the vortex control study will then be applied to the SOA 45^o, which requires less actuator energy than the Coanda configurations.

Eventually it is desired to eliminate the need to gate the signal by tuning the natural frequency of the oscillator to the natural shedding frequency. This is expected to also require a method of phase synchronization . Currently the phase of each oscillator in the array is random, and in order to influence the shear layer it is expected that a coherent signal must be developed across the array. Methods for phase synchronization are currently being studied as a larger effort within the research group.

The are several improvements that can be made to the experimental setup. One improvement would be the use of a six component load cell to also measure lift and moments. This will also reduce the systematic error caused by model vibration, as discussed earlier, and give higher measurement repeatability. This will also reduce the amount of time needed to calibrate the model. Such a system was not within the budget of the current study.

Summary

In conclusion, an Ahmed model was used to test fluidic oscillators as flow control actuators for reducing drag. A drag reduction of 7% is seen on the 25^{o} slant. This thought to be due to reduction of the separation bubble and modification of the torus structure. The higher angle configurations proved to be more challenging. Streamwise vortices possibly lead to a drag increase on these configurations, emphasizing that multiple control strategies should be applied simultaneously. Future flow control approaches must address the 3-D complexity associated with this flow.

References:

1.) Hucho, W. Heinrich, Aerodynamics of Road Vehicles p.104, 1998.

2.) Ahmed, S.R., "Some salient features of the time averaged vehicle wake", SAE 1984.

3.) Ruomeas, Mathieu et al., "Drag reduction by flow separation control on a car after body.", International Journal of Numerical Methods Fluids (2009), 60:1222-1240.

4.) Littlewood, R.P.,"Aerodynamic drag reduction of a simplified squareback vehicle using steady blowing", Experimental Fluids, 2012.

5.)Geropp, D. and H.-J. Odenthal, "Drag reduction of motor vehicles by active flow control using the Coanda effect.", Experiments in Fluids 28 (200) 74-85

6.) Gregory, James, et al. "Characterization of a Micro Fluidic Oscillator for Flow Control." 2nd AIAA Flow Control Conference, AIAA (2004) Article 2692.

7.) Bayraktar I, Landman D, Baysal O ,"Experimental and computational investigation of Ahmed body for ground vehicle aerodynamics." In: Proceedings of the SAE international truck and bus meeting and exhibition, Chicago, (2001) SAE paper 2001-01-2742.

8.) Lajos, Tamas, "Drag reduction by the production of a separation bubble on the fron of a bluff body." Journal of Wind Engineering and Industrial Aerodynamics, 22 (1986) 331-338.

9.) Brunn, A. and Nitsche W., "Drag reduction of an Ahmed car model by means of active separation control on at the rear slant", Institute of Aeronautics and Astronautics, Technical University Berlin.

10.)Joseph Pierric et al, "Drag reduction on the 25^{o} slant angle Ahmed reference body using pulsed jets" Experimental Fluids, (2012) 52:1169-1185.

11.) wikipedia.org/Automobile_drag_coefficient.html

12.) Conan et al., "Experimental aerodynamic study of a car type bluff body", Experimental Fluids, (2011) 50:1273-1284.

13.) Ahmed, S.R and Ramm, G., "Some salient features of the time-averaged ground vehicle wake", (1984) SAE technical paper TP840300.

14.) Fago, B., Lindher, H., Mahrenholtz, O., 1991, "The effect of ground simulation on the flow around vehicles in wind tunnel testing," J. of Wind Engineering and Industrial Aerodynamics, Vol.38, pp.47-57

15.) Raghu, S., "Fluidic oscillators for flow control", Experimental Fluids, (2013), 54:1455

16.) Kiya M, Sasaki K (1985) Structure of large scale vortices and unsteady reverse flow in the reattaching zone of a turbulent separation bubble. J Fluid Mech 154:463–491

17.) Brunn et al., "Active drag control for a generic car model", (2007) NNFM 95:247-259.

18.) Pastoor, Mark et al., "Feedback shear layer control for bluff body drag reduction.", Journal of Fluid Mechanics, (2008) 608:161-196.

Appendix A: Additional hotwire data for SOA configurations.

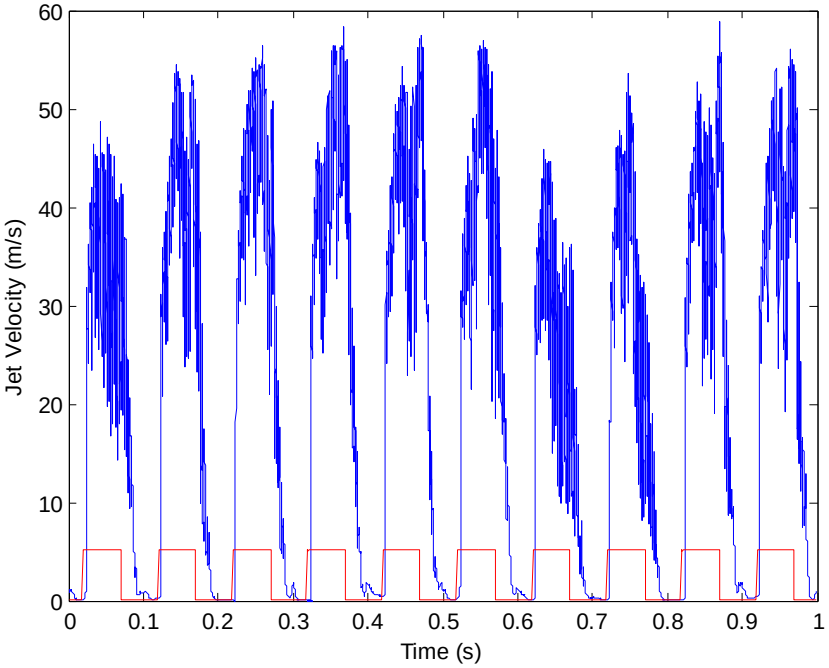

35 L/min, 10 Hz, 50% duty cycle

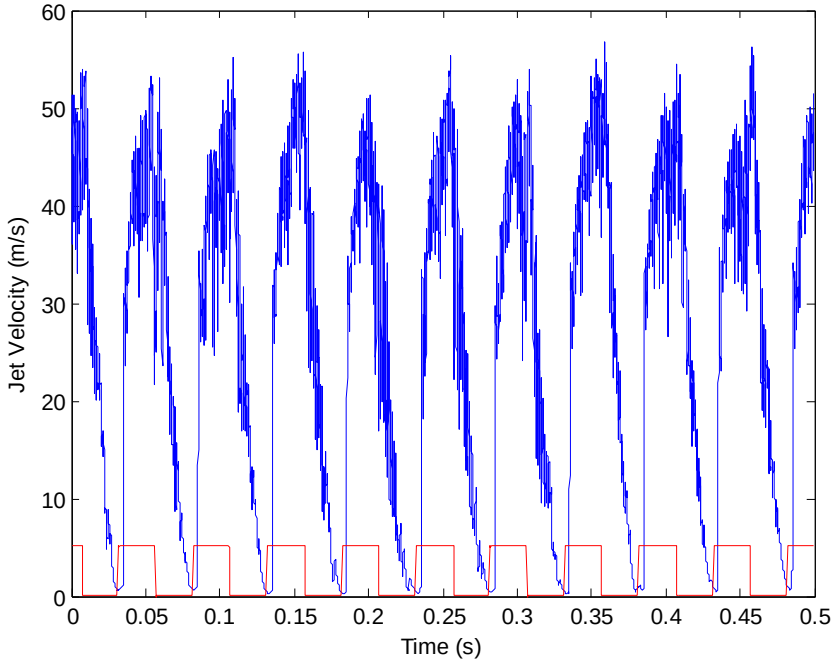

35 L/min, 20 Hz, 50% duty cycle

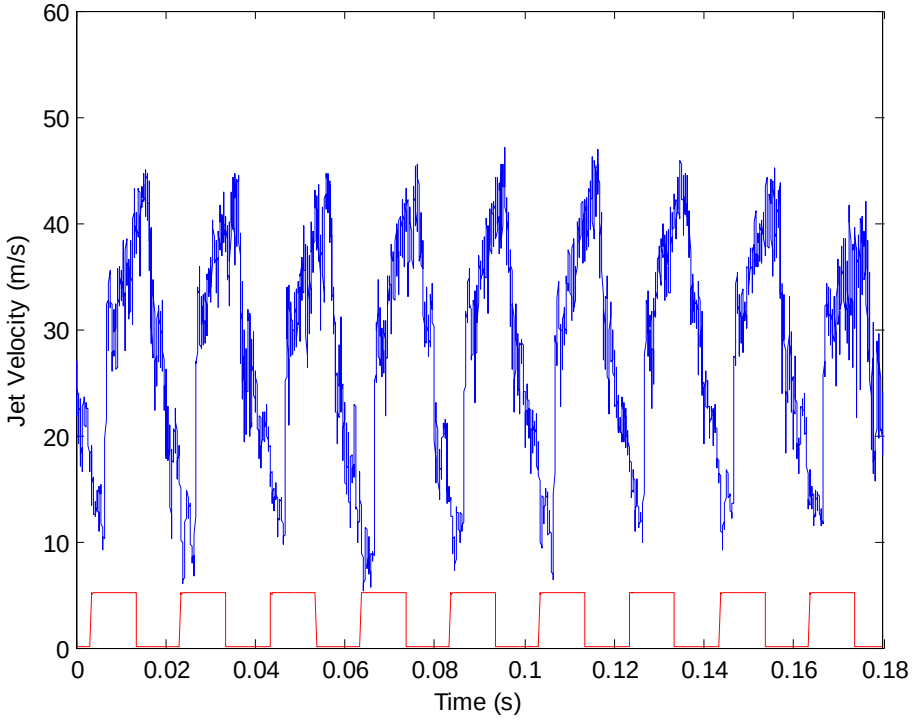

35 L/min, 50 Hz, 50%duty cycle

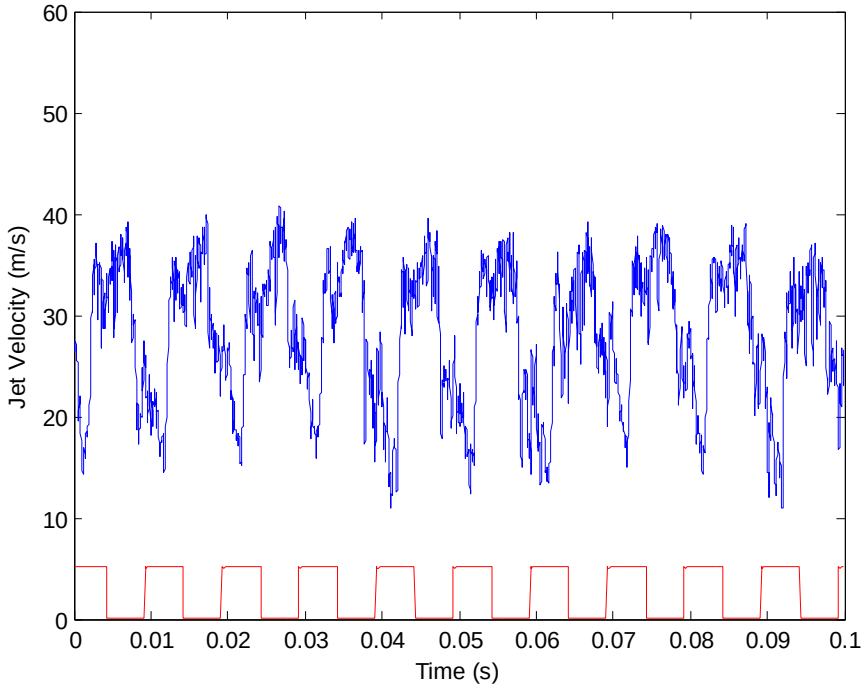

35 L/min, 10t20 Hz, 50%duty cycle

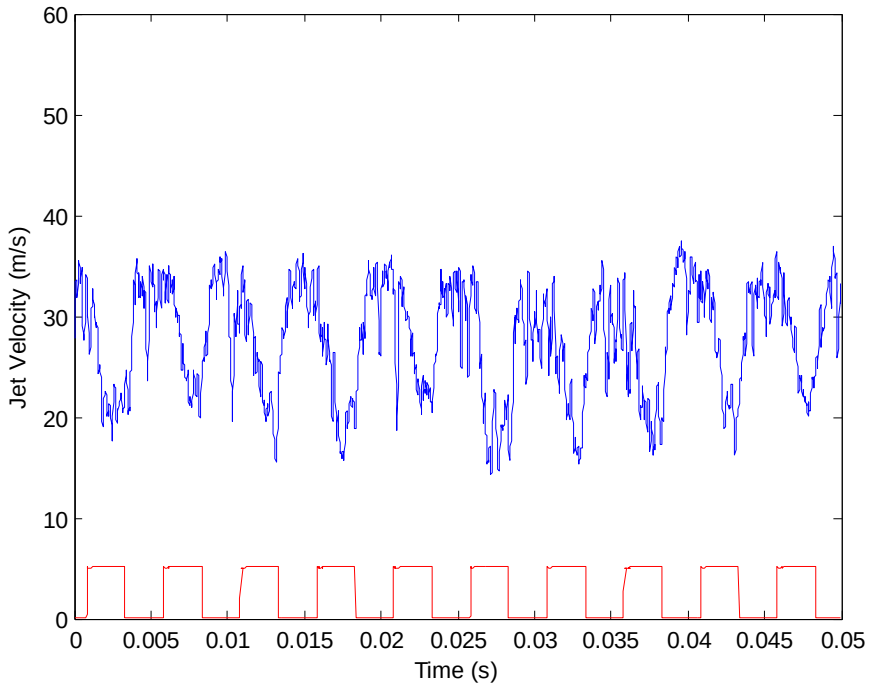

35 L/min, 200 Hz, 50%duty cycle

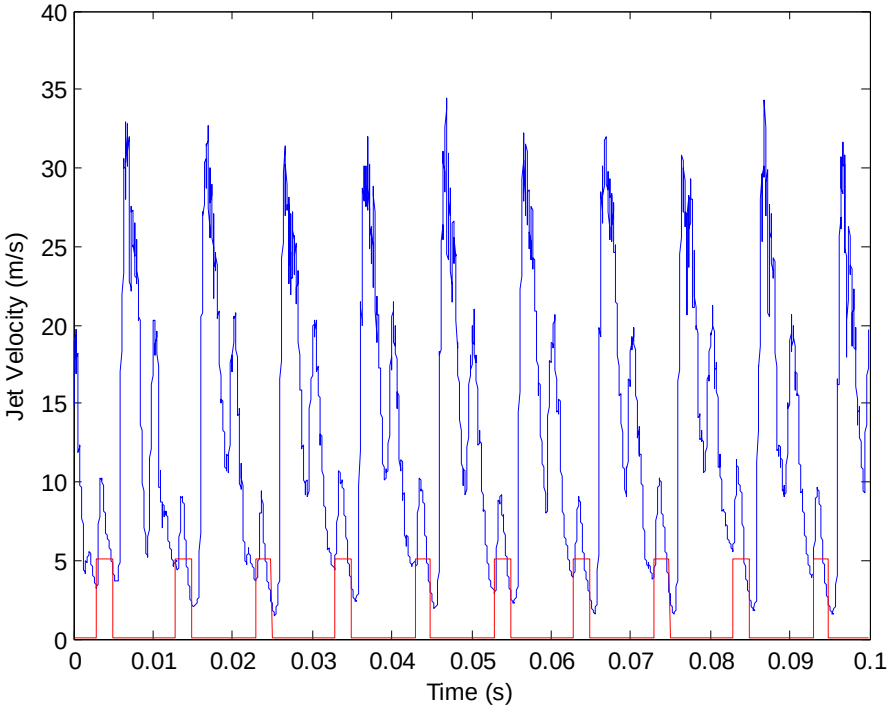

20 L/min, 100 Hz, 50%duty cycle

Appendix B: Additional model and actuator details

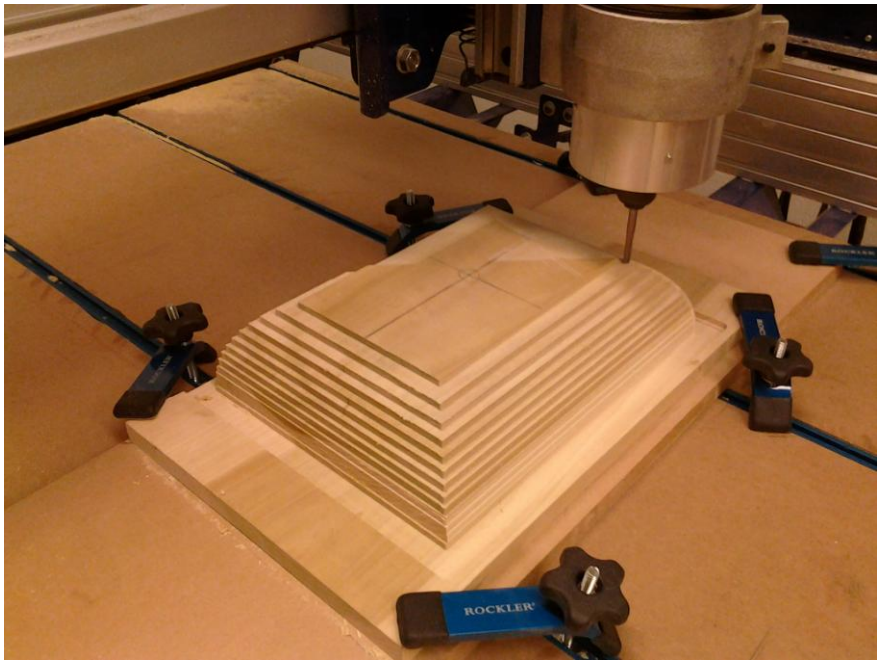

CNC router used to create model nose.

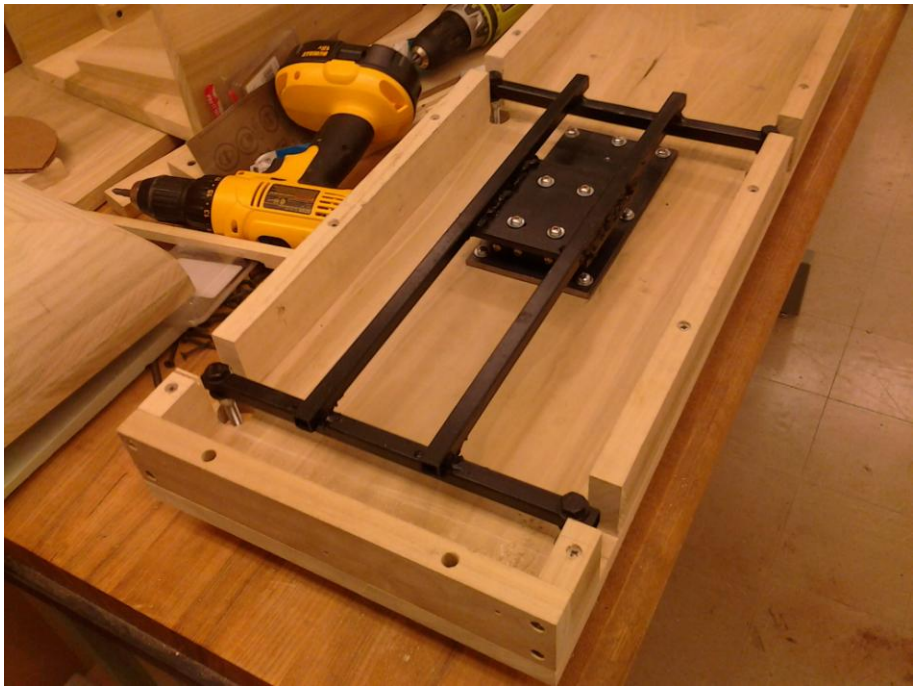

Additional image of the linear stage system.

Insert for actuator in slant piece.

Slant piece with baseline insert.

Inside of removable slant piece.

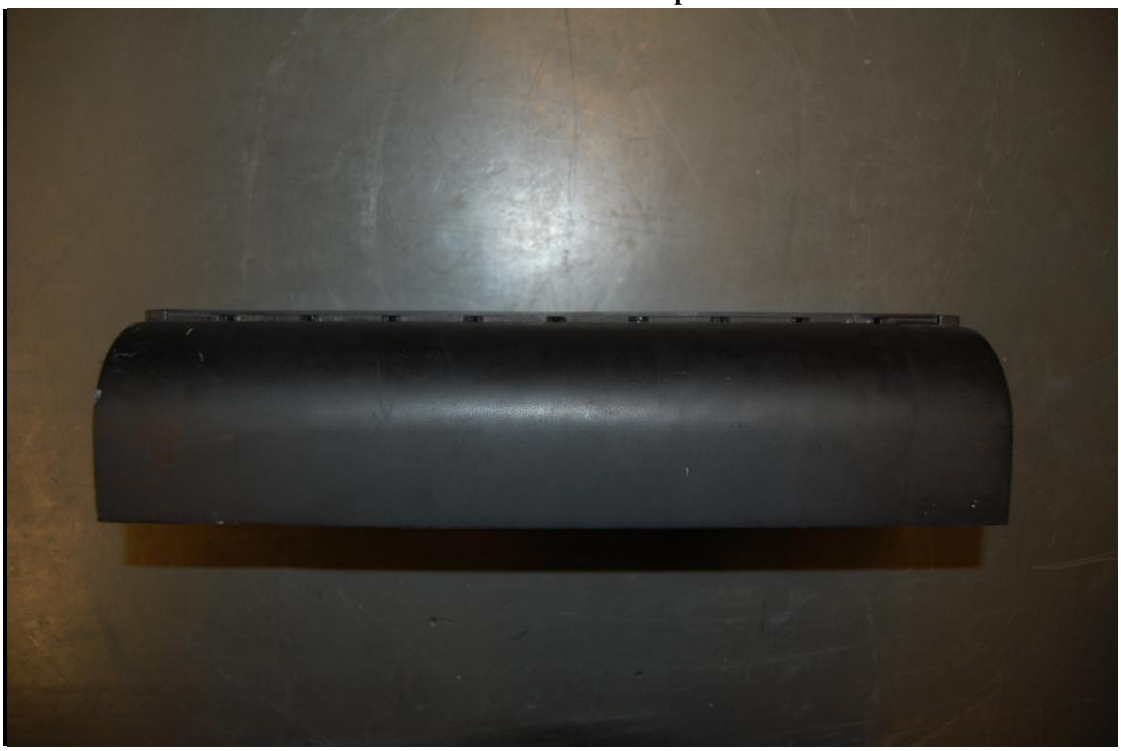

90^{o} coanda piece, this shows the oscillator outlets.

Back of the 90^{o} coanda piece. Notice the 9 mm laser cut acrylic pieces, laminated to form the surface.

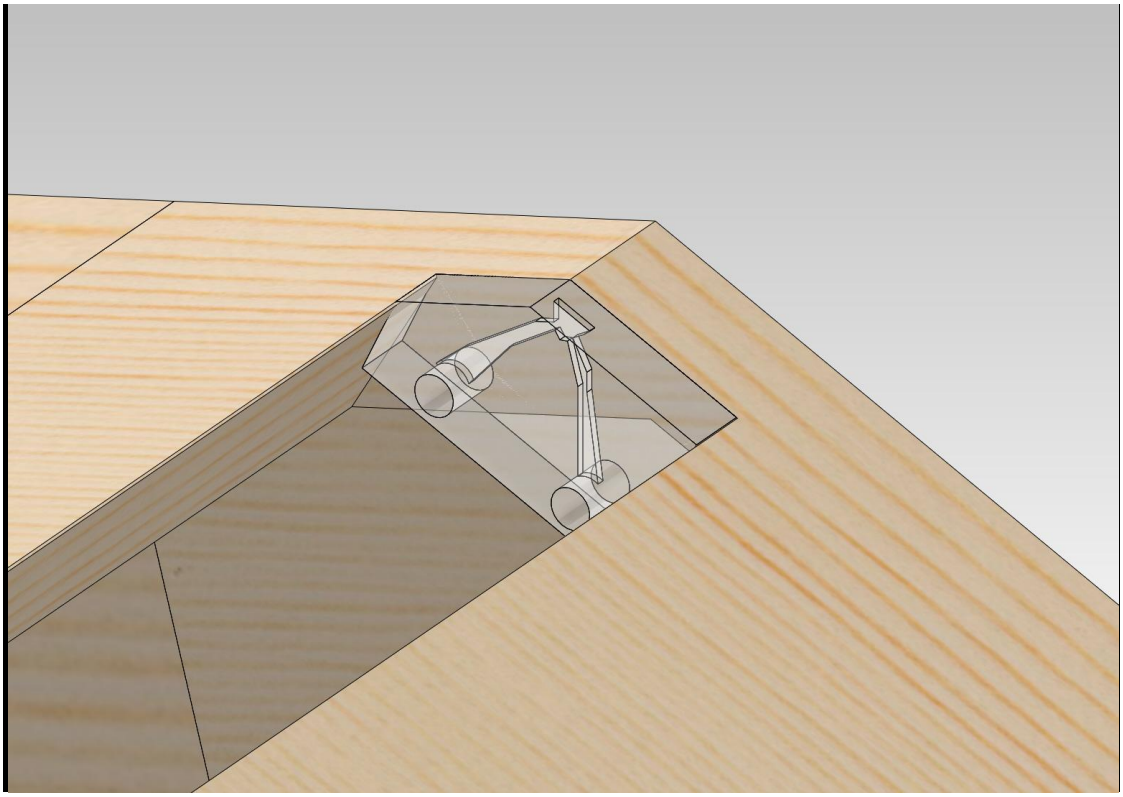

Streamwise oscillating jet concept (briefly mentioned in the "other configurations" section)

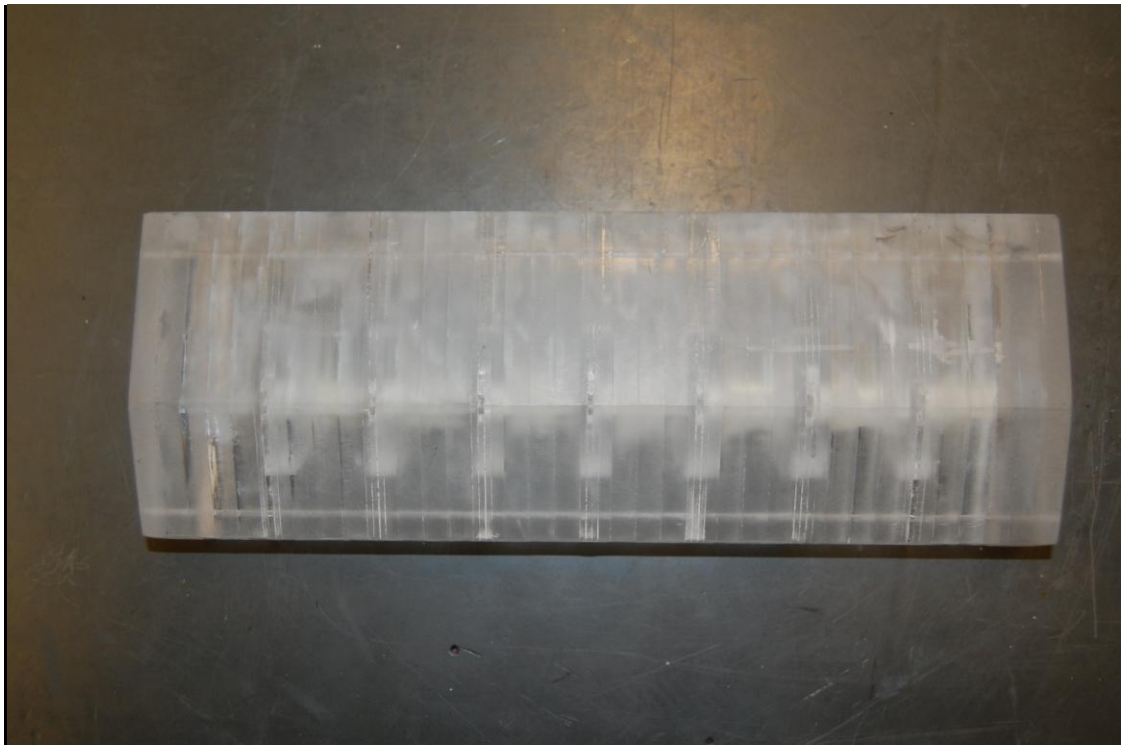

Streamwise oscillating jet for the 25^{o} slant

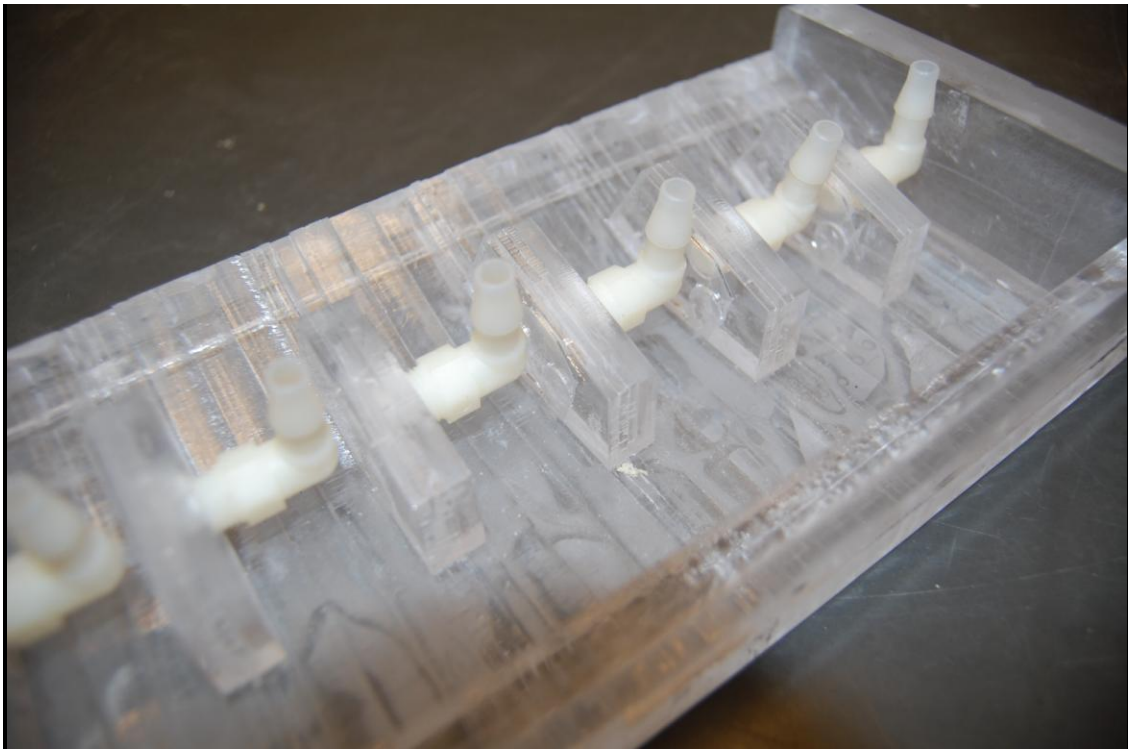

Further detail of the streamwise oscillating jet for the 25^{o} slant

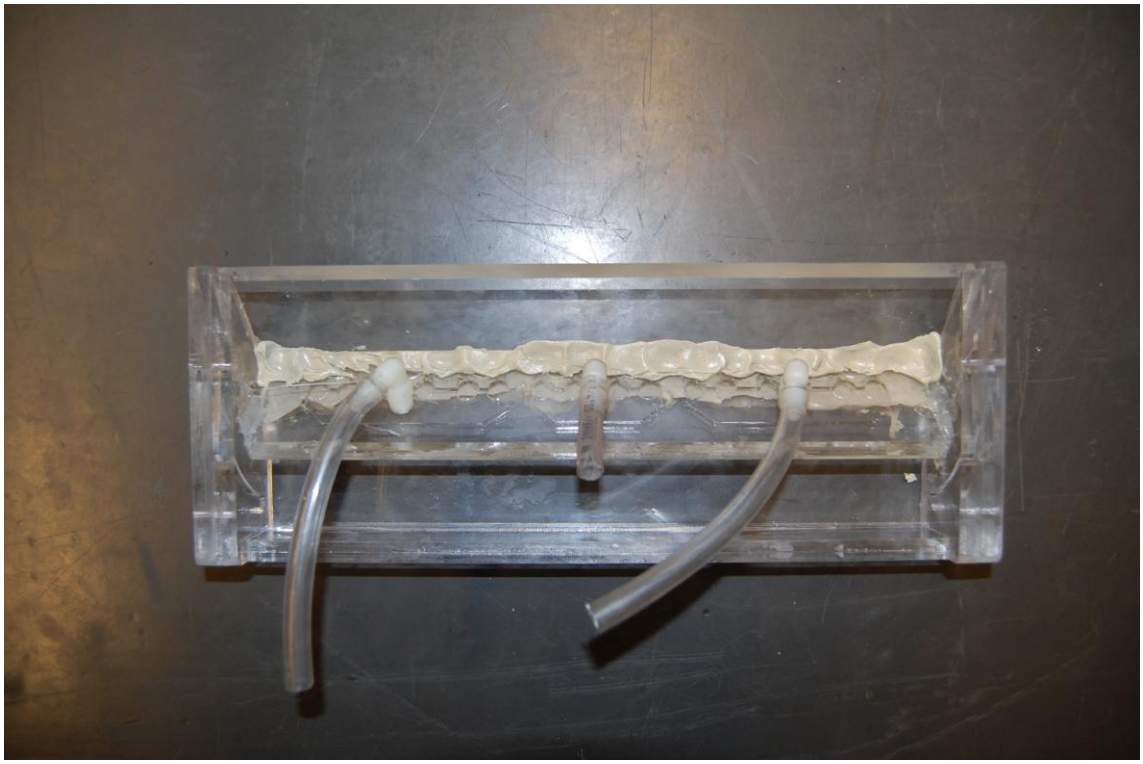

SOA configuration for the 45^{o} slant, the other angles are similar.

Oscillator at the edge of a 25^{o} slant insert. (An initial attempt at vortex control.)

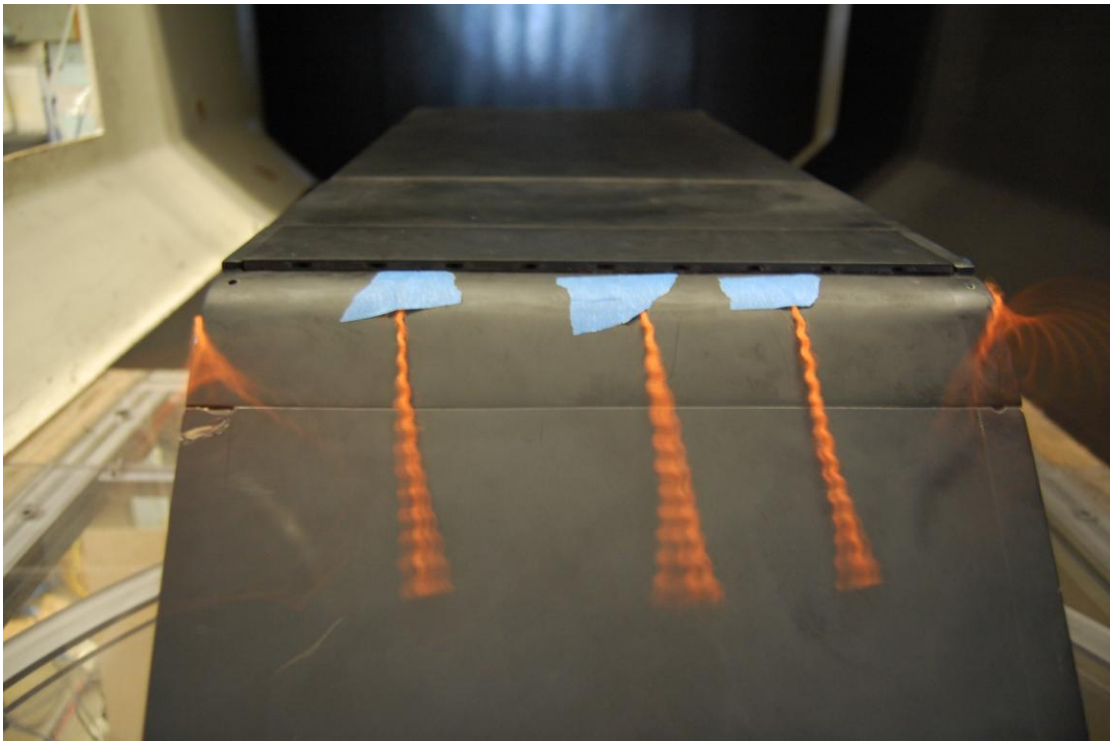

Vortices on the 45^{o} Coanda configuration.

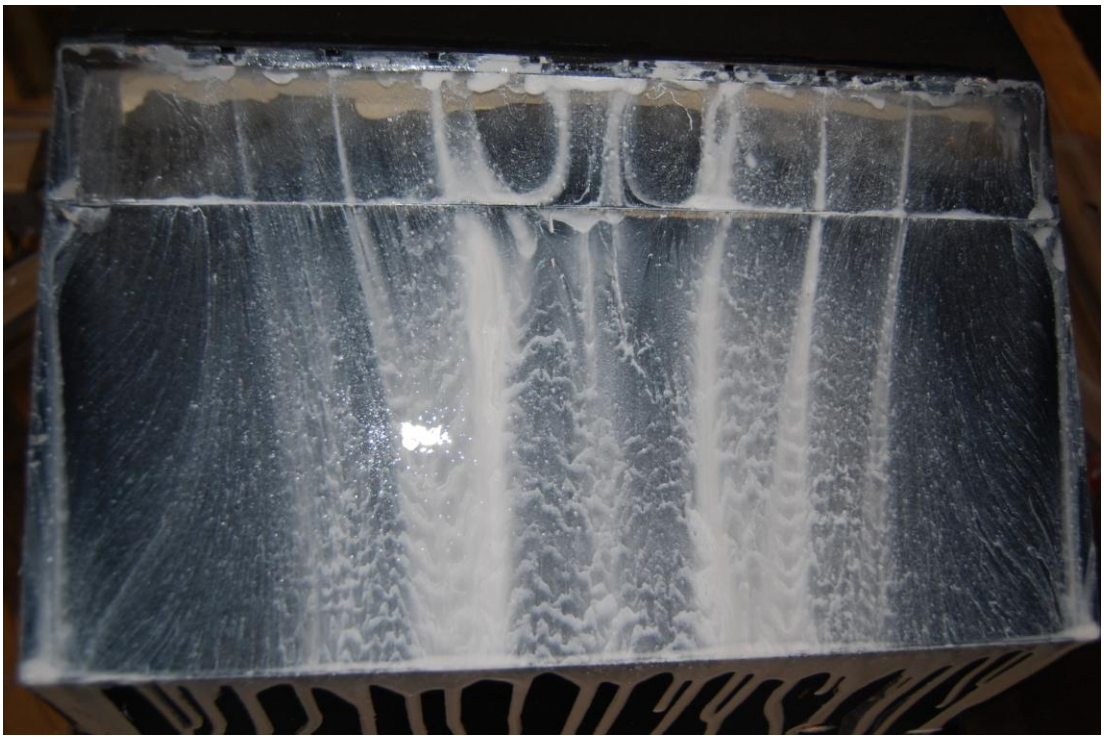

An attempt at oil flow visualization using titanium dioxide pigment. Notice the outline of the vortices on the side edges of this 25^{o} slant.